

## **Supporting Information**

# **Tailoring 3D-printed Electrodes for Enhanced Water Splitting**

*Raúl A. Márquez,<sup>†</sup> Kenta Kawashima,<sup>†</sup> Yoon Jun Son,<sup>††</sup> Roger Rose,<sup>‡</sup> Lettie A. Smith,<sup>†</sup>  
Nathaniel Miller,<sup>‡‡</sup> Omar Ali Carrasco Jaim,<sup>††</sup> Hugo Celio,<sup>§</sup> and C. Buddie Mullins<sup>†,††,§,§§,¶,\*</sup>*

<sup>†</sup> Department of Chemistry, The University of Texas at Austin, Austin, Texas 78712, United States.

<sup>††</sup> McKetta Department of Chemical Engineering, The University of Texas at Austin, Austin, Texas 78712, United States.

<sup>‡</sup> Texas Inventionworks, The University of Texas at Austin, Austin, Texas 78712, United States.

<sup>‡‡</sup> Jackson School of Geosciences, The University of Texas at Austin, Texas 78712, United States.

<sup>§</sup> Texas Materials Institute, The University of Texas at Austin, Texas 78712, United States.

<sup>§§</sup> Center for Electrochemistry, The University of Texas at Austin, Austin, Texas 78712, United States.

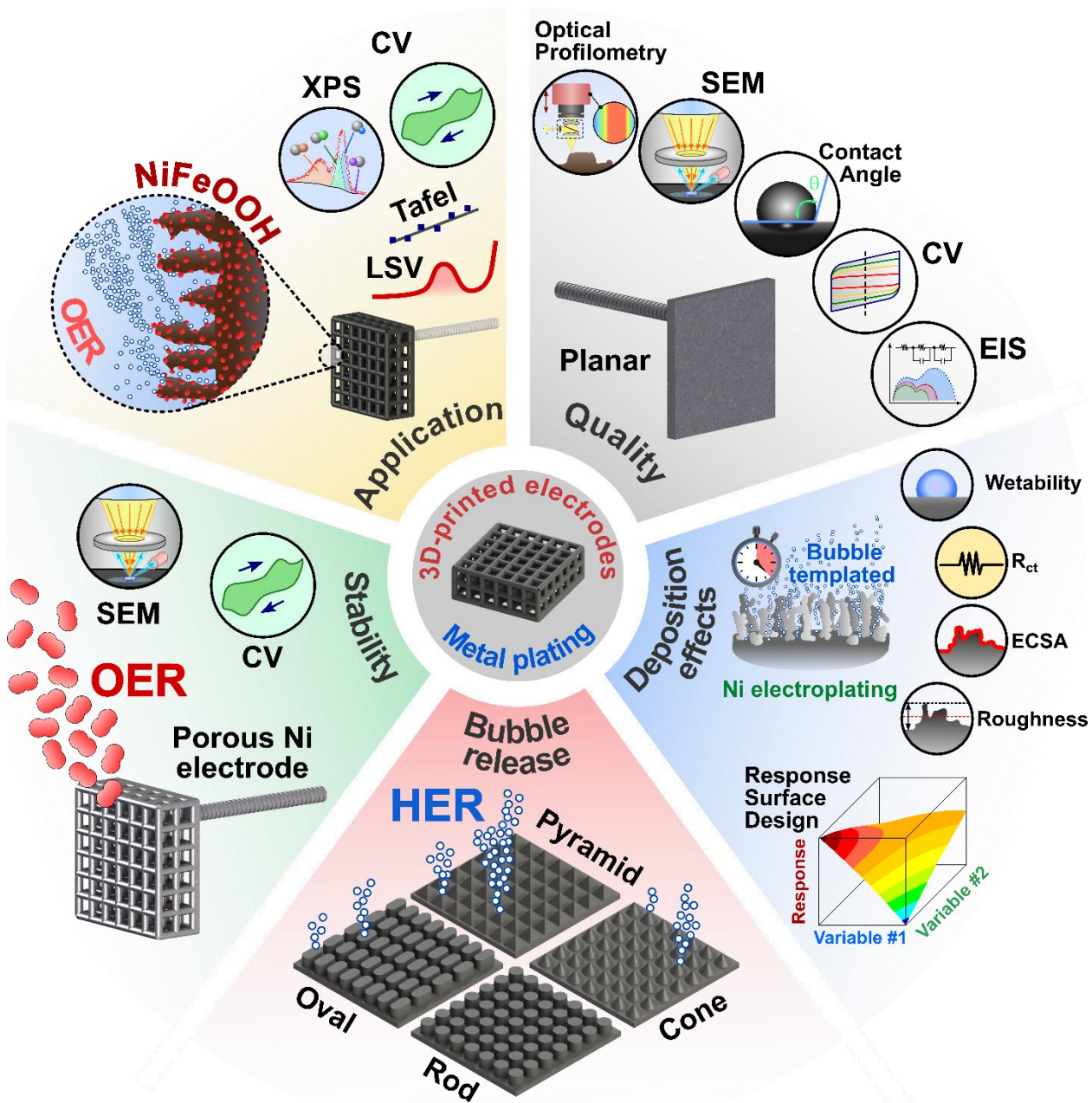
<sup>¶</sup> H2@UT, The University of Texas at Austin, Texas 78712, United States.

\* Corresponding author: [mullins@che.utexas.edu](mailto:mullins@che.utexas.edu)

Number of pages: 48

Number of figures (including schemes): 42

Number of tables: 3



**Scheme S1.** Characterization approaches for evaluating the 3D-printed electrodes in this study.

**Table S1.** Dimensions and pictures of the examined 3D-printed electrode architectures.

Electrode	Planar	Cone	Pyramid	Rod	Oval	3D Porous
Total area (cm <sup>2</sup> )	14.6790	22.7342	25.2600	21.1969	21.7265	48.0042
Exposed Area (cm <sup>2</sup> )	8.2500	16.4842	19.0100	14.9469	15.4765	47.8042
Photo (SLS)						
Photo (Cu)						
Photo (Ni)						
Dimensions						
L (mm)	25	25	25	25	25	25
W (mm)	25	25	25	25	25	25
D (mm)	2	1	1	1	1	9.75
r (mm)	-	1.5	-	1.25	-	-
h (mm)	-	2	2	2	2	-
a (mm)	-	-	3	-	2	2.5
b (mm)	-	-	-	-	4	2.5

**Note:** total area refers to the full surface geometric surface calculated from the 3D model in SolidWorks, while the *exposed area* refers to the total area exposed to the electrolyte (*i.e.*, subtracting the area covered by seals and gaskets). We use this *exposed area* as the “geometric” area instead of the “projected” area (25 × 25 mm<sup>2</sup> square, which is the same for all the electrodes).

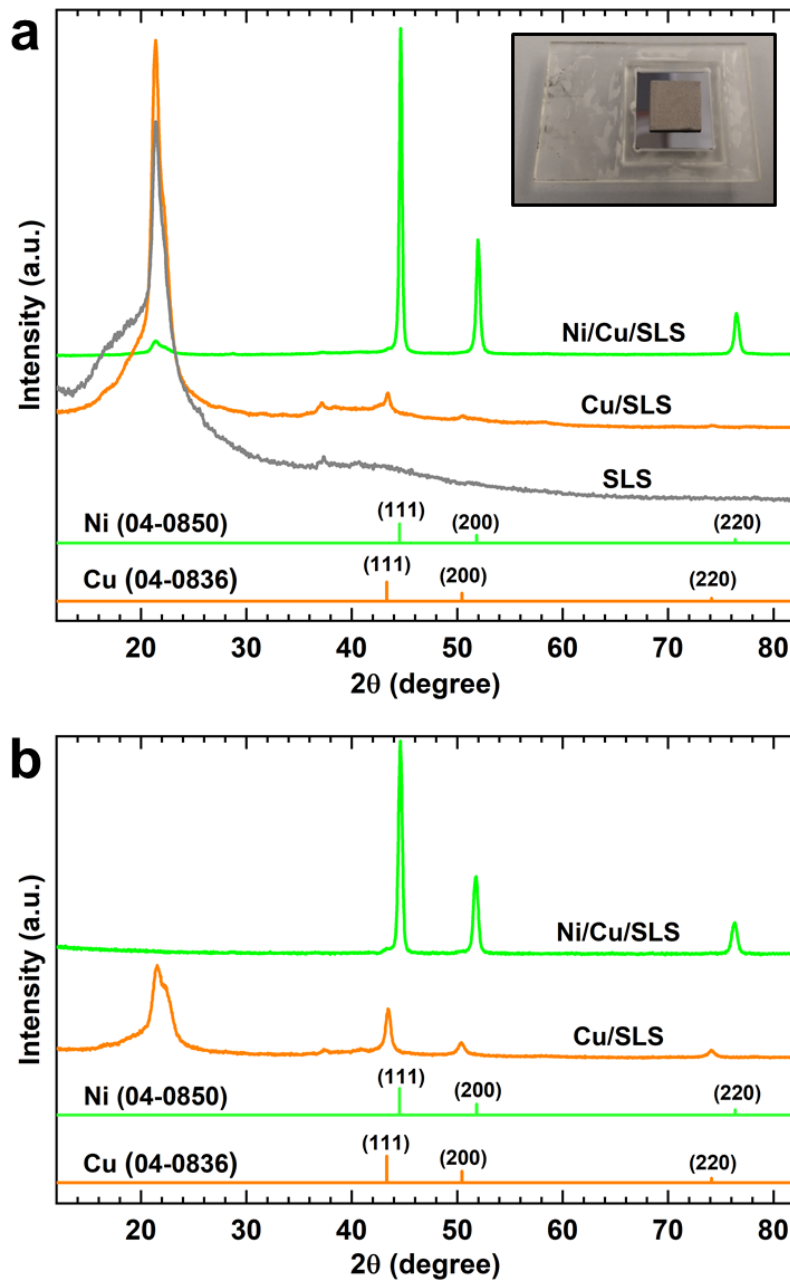


**Figure S1.** XRD patterns of the as-printed electrodes: (a) typical XRD measurements of nylon (SLS), Cu-coated (Cu/SLS), and Ni-coated (Ni/Cu/SLS) planar electrodes (inset: picture of the 3D-printed plastic holder equipped with a Si wafer), (b) GIXRD measurements of Cu/SLS and Ni/Cu/SLS planar electrodes.

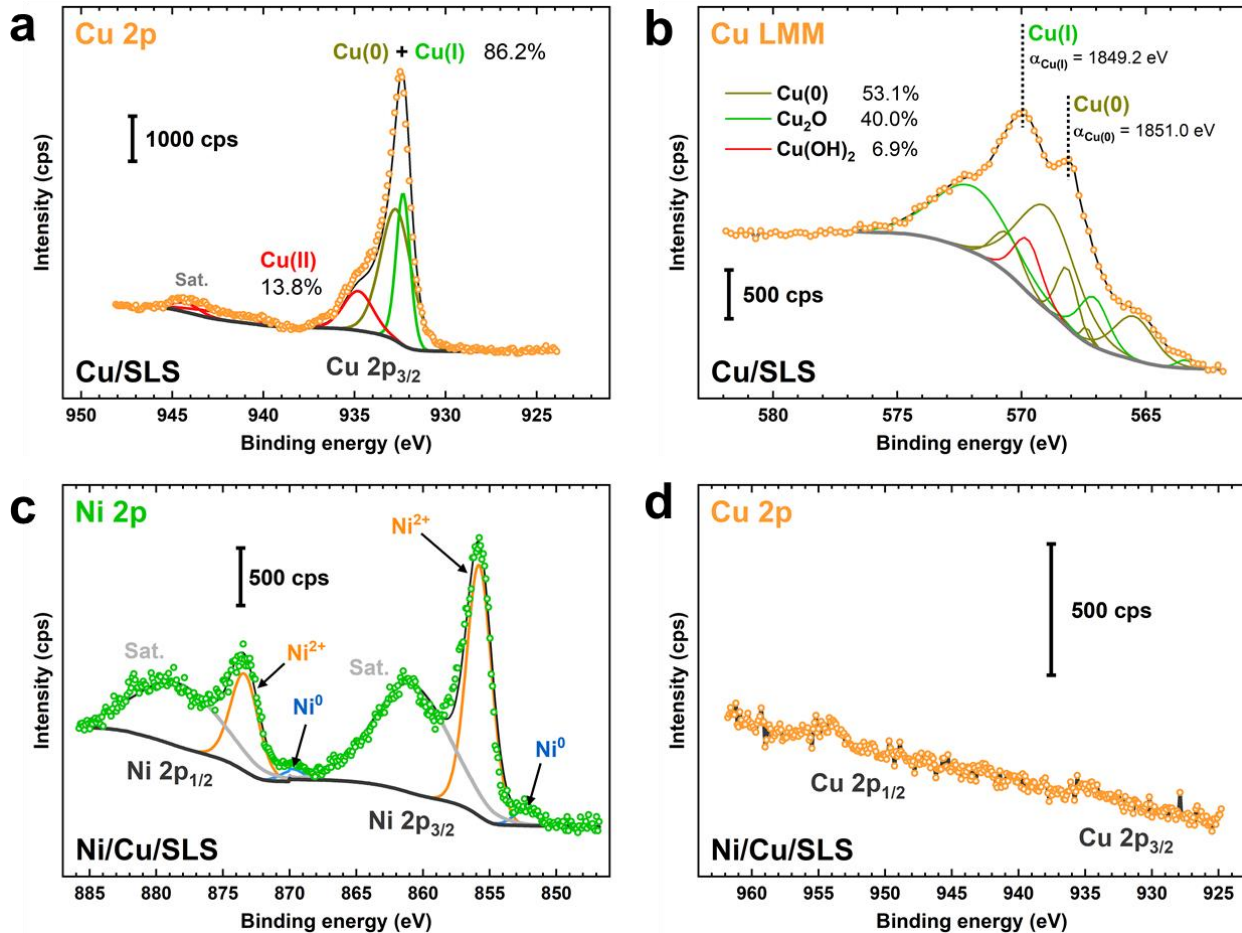


**Figure S2.** XPS analysis of the metal-coated electrodes: (a) Cu 2p<sub>3/2</sub> and (b) Cu LMM spectra of the Cu/SLS electrode, (c) Ni 2p and (d) Cu 2p spectra of the Ni/Cu/SLS electrode.

We estimated the modified Auger parameters of Cu(0) and Cu<sub>2</sub>O according to the equation:

$$\alpha_{\text{Cu}} = \text{BE}_{\text{Cu } 2p_{3/2}} + (\hbar v - \text{BE}_{\text{Cu LMM}})$$

where BE<sub>Cu 2p<sub>3/2</sub></sub> refers to the binding energy at the Cu 2p<sub>3/2</sub> peak maximum,  $\hbar v$  represents the beam energy (Al source: 1468.6 eV), and BE<sub>Cu LMM</sub> refers to the Cu LMM peak maximum. From **Figure S2a**, BE<sub>Cu 2p<sub>3/2</sub></sub> = 932.5 eV. From **Figure S2b**, BE<sub>Cu LMM</sub> = 568.2 eV and 569.9 eV for the Cu(0) and Cu(I) peaks, respectively. The estimated modified Auger parameters are shown in **Figure S2b**, which are in accordance with the literature values for Cu(0) and Cu<sub>2</sub>O.<sup>1</sup>

We also estimated the Cu composition from the Cu 2p and Cu LMM spectra using the curve-fitting parameters reported by Biesinger.<sup>1</sup> Curve fitting of the Cu LMM spectrum effectively resolved contributions from Cu(0) and Cu<sub>2</sub>O. Presence of Cu<sub>2</sub>O and Cu(OH)<sub>2</sub> on the surface can be attributed to surface oxidation as the samples were exposed to air.<sup>2</sup> Nevertheless, both Cu 2p and Cu LMM spectra show that the major component was Cu(0).

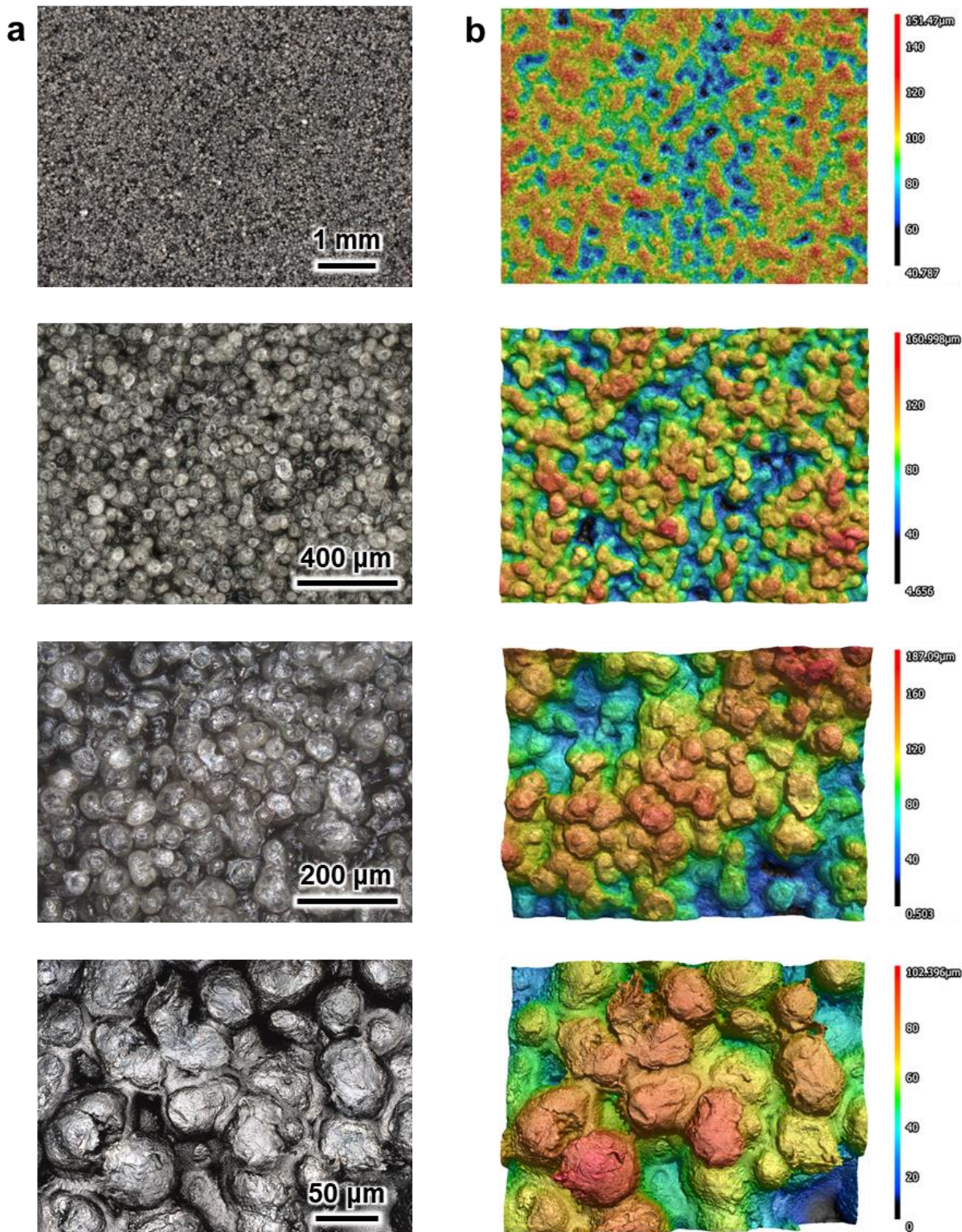


**Figure S3.** Additional NCP images of the planar Nylon electrode at different magnifications: (a) optical images and (b) surface color maps. Color scales correspond to height.

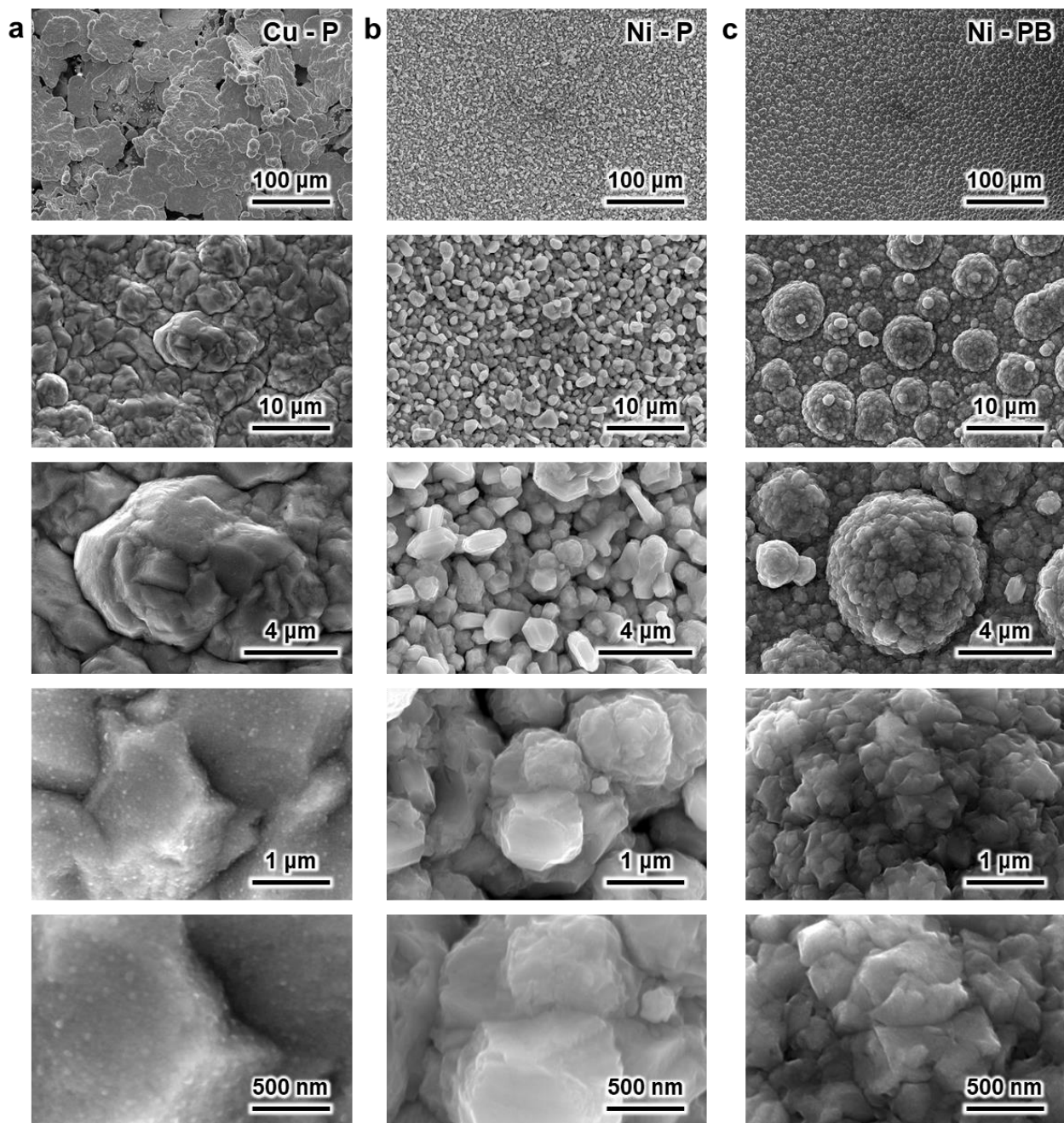


**Figure S4.** Additional SEM images of planar electrodes at different magnifications: (a) Cu-P, (b) Ni-P, and (c) Ni-PB electrodes.

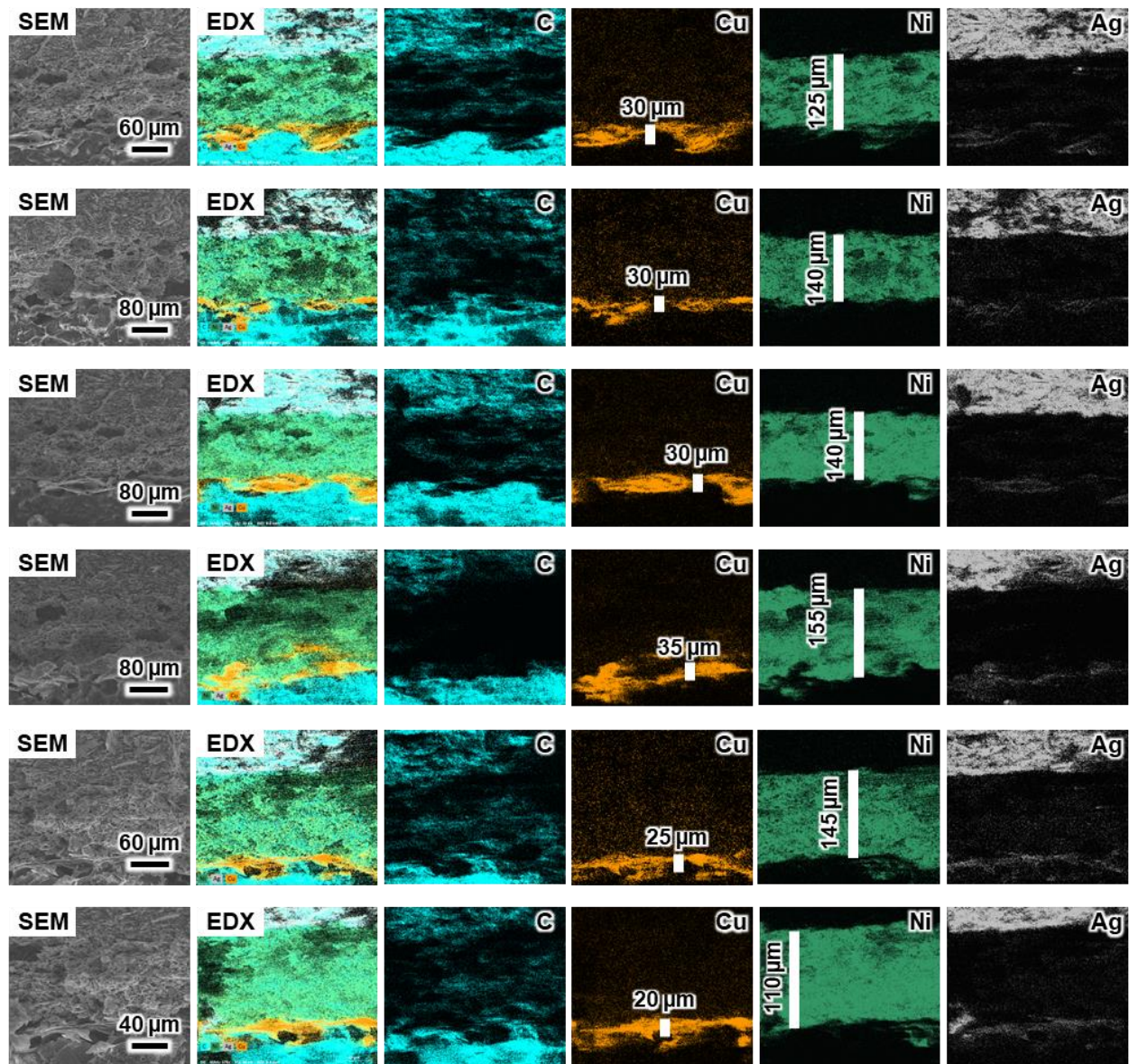


**Figure S5.** Additional EDX elemental mappings of cross-sectional cuts of Ni-PB electrodes.

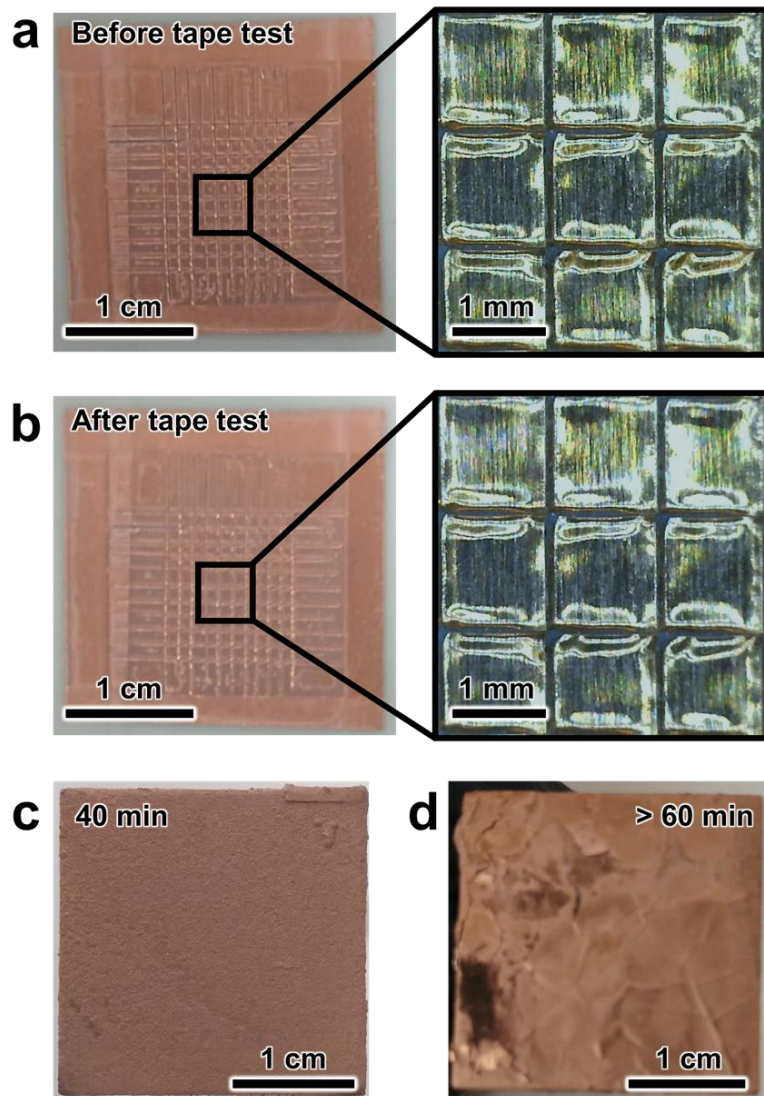


**Figure S6.** Adhesion of the as-deposited Cu coating (40 min) on Nylon substrates according to the tape test (ASTM D3359): optical microscope images taken (a) before and (b) after peeling off a piece of Scotch tape from the Cu film. Pictures of Cu-coated nylon planar electrodes after (c) 40 min and (d) 60 min deposition. Tape test procedure adapted from Ref.<sup>3</sup>.

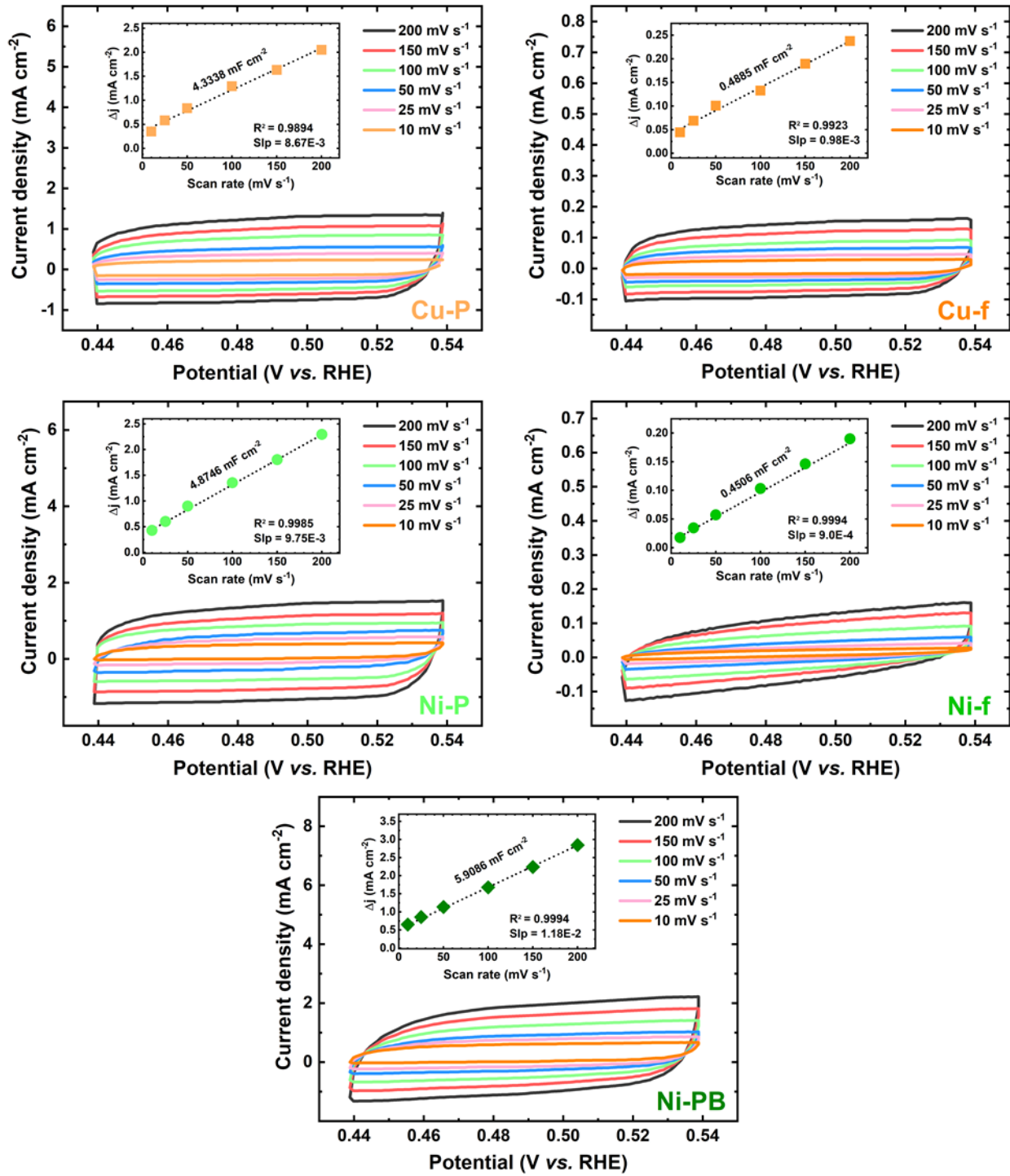


**Figure S7.** CV scans in the non-faradaic region at different scan rates for estimating the double-layer capacitance ( $C_{dl}$ ) of as-prepared electrodes (*i.e.*, Cu-P, Ni-P, and Ni-PB) and smooth metal foils (*i.e.*, Cu-f, Ni-f) used as control samples.

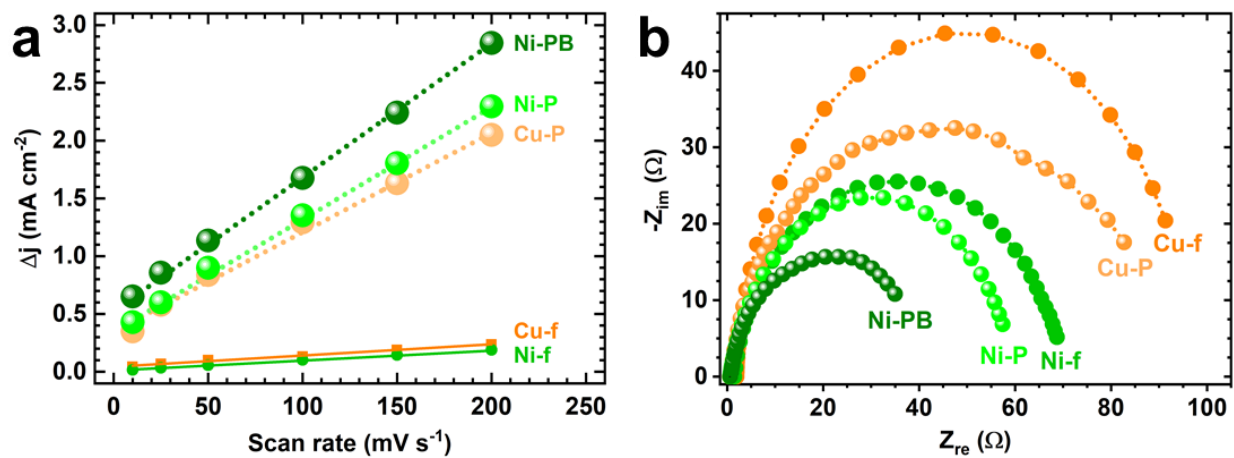


**Figure S8.** Additional electrochemical characterization plots for metal-coated planar electrodes: (a) double-layer capacitance comparison plot for electrodes displayed in Figure S7, (b) Nyquist plots from EIS measurements for each planar electrode.

**Table S2.** Coded coefficients, analysis of variance, and regression models for Ni electrodeposition surface mappings using the RSM experimental design. Note: *Dep2* refers to the second deposition time, whereas *Dep3* refers to the third deposition time.

## Contact Angle

### Coded Coefficients

Term	Coef	T-Value	P-Value
Constant	42.064	43.48	0.000
Dep2	-6.318	-8.26	0.000
Dep3	-3.839	-5.02	0.000
Dep2*Dep2	11.377	13.87	0.000
Dep3*Dep3	8.567	10.45	0.000
Dep2*Dep3	-2.44	-2.25	0.028

### Model Summary

S	R-sq	R-sq(adj)	R-sq(pred)
4.83666	96.15%	94.97%	92.34%

### Analysis of Variance

Source	DF	Adj SS	F-Value	P-Value
Model	5	8582.1	73.37	0.000
Linear	2	2186.5	46.73	0.000
Dep2	1	1596.9	68.26	0.000
Dep3	1	589.6	25.20	0.000
Square	2	6277.0	134.16	0.000
Dep2*Dep2	1	4501.9	192.45	0.000
Dep3*Dep3	1	2552.7	109.12	0.000
2-Way	1	118.6	5.07	0.028
Interaction				
Dep2*Dep3	1	118.6	5.07	0.028
Error	59	1380.2		
Lack-of-Fit	3	667.5	17.48	0.000
Pure Error	56	712.7		
Total	64	9962.3		

### Regression Equation

$$\theta = 108.79 - 2.729 \text{Dep2} - 1.925 \text{Dep3} \\ + 0.05160 \text{Dep2*Dep2} + 0.03885 \text{Dep3*Dep3} \\ - 0.01104 \text{Dep2*Dep3}$$

### Double-layer capacitance

Term	Coef	T-Value	P-Value
Constant	6.1616	227.21	0.000
Dep2	0.2177	10.15	0.000
Dep3	0.3038	14.17	0.000
Dep2*Dep2	-0.2661	-11.57	0.000
Dep3*Dep3	-0.2883	-12.54	0.000
Dep2*Dep3	-0.0460	-1.52	0.135

### Model Summary

S	R-sq	R-sq(adj)	R-sq(pred)
0.135592	90.53%	89.73%	88.09%

### Analysis of Variance

Source	DF	Adj SS	F-Value	P-Value
Model	5	10.3671	112.78	0.000
Linear	2	5.5864	151.93	0.000
Dep2	1	1.8952	103.08	0.000
Dep3	1	3.6913	200.77	0.000
Square	2	4.7383	128.86	0.000
Dep2*Dep2	1	2.4628	133.96	0.000
Dep3*Dep3	1	2.8909	157.24	0.000
2-Way	1	0.0423	2.30	0.135
Interaction				
Dep2*Dep3	1	0.0423	2.30	0.135
Error	59	1.0847		
Lack-of-Fit	3	0.6029	23.36	0.000
Pure Error	56	0.4818		
Total	64	11.4518		

### Regression Equation

$$C_{dl} = 3.582 + 0.08021 \text{Dep2} + 0.09105 \text{Dep3} \\ - 0.001207 \text{Dep2*Dep2} \\ - 0.001307 \text{Dep3*Dep3} \\ - 0.000209 \text{Dep2*Dep3}$$

## Charge transfer resistance

### Coded Coefficients

Term	Coef	T-Value	P-Value
Constant	45.120	160.31	0.000
Dep2	-6.003	-26.98	0.000
Dep3	-3.064	-13.77	0.000
Dep2*Dep2	3.081	12.91	0.000
Dep3*Dep3	2.834	11.88	0.000
Dep2*Dep3	-0.535	-1.70	0.094

### Model Summary

S	R-sq	R-sq(adj)	R-sq(pred)
1.40722	95.29%	94.89%	93.99%

### Analysis of Variance

Source	DF	Adj SS	F-Value	P-Value
Model	5	2362.17	238.57	0.000
Linear	2	1817.03	458.78	0.000
Dep2	1	1441.63	727.99	0.000
Dep3	1	375.40	189.57	0.000
Square	2	539.42	136.20	0.000
Dep2*Dep2	1	330.08	166.69	0.000
Dep3*Dep3	1	279.37	141.08	0.000
2-Way	1	5.72	2.89	0.094
Interaction				
Dep2*Dep3	1	5.72	2.89	0.094
Error	59	116.84		
Lack-of-Fit	3	72.91	30.98	0.000
Pure Error	56	43.93		
Total	64	2479.01		

### Regression Equation

$$R_{ct} = 75.63 - 1.0422 \text{ Dep2} - 0.7883 \text{ Dep3} \\ + 0.01397 \text{ Dep2*Dep2} + 0.01285 \text{ Dep3*Dep3} \\ - 0.00243 \text{ Dep2*Dep3}$$

## Root mean squared roughness

### Coded Coefficients

Term	Coef	T-Value	P-Value
Constant	17.159	72.65	0.000
Dep2	1.721	9.21	0.000
Dep3	1.651	8.84	0.000
Dep2*Dep2	-1.834	-9.16	0.000
Dep3*Dep3	-2.441	-12.19	0.000
Dep2*Dep3	2.612	9.89	0.000

### Model Summary

S	R-sq	R-sq(adj)	R-sq(pred)
1.18096	94.80%	92.85%	91.77%

### Analysis of Variance

Source	DF	Adj SS	F-Value	P-Value
Model	5	652.428	93.56	0.000
Linear	2	227.410	81.53	0.000
Dep2	1	118.426	84.91	0.000
Dep3	1	108.983	78.14	0.000
Square	2	288.531	103.44	0.000
Dep2*Dep2	1	116.978	83.87	0.000
Dep3*Dep3	1	207.265	148.61	0.000
2-Way	1	136.487	97.86	0.000
Interaction				
Dep2*Dep3	1	136.487	97.86	0.000
Error	59	82.285		
Lack-of-Fit	3	1.729	0.40	0.753
Pure Error	56	80.556		
Total	64	734.714		

### Regression Equation

$$RMS = 6.77 + 0.2355 \text{ Dep2} + 0.3685 \text{ Dep3} \\ - 0.008317 \text{ Dep2*Dep2} \\ - 0.011071 \text{ Dep3*Dep3} \\ + 0.01185 \text{ Dep2*Dep3}$$

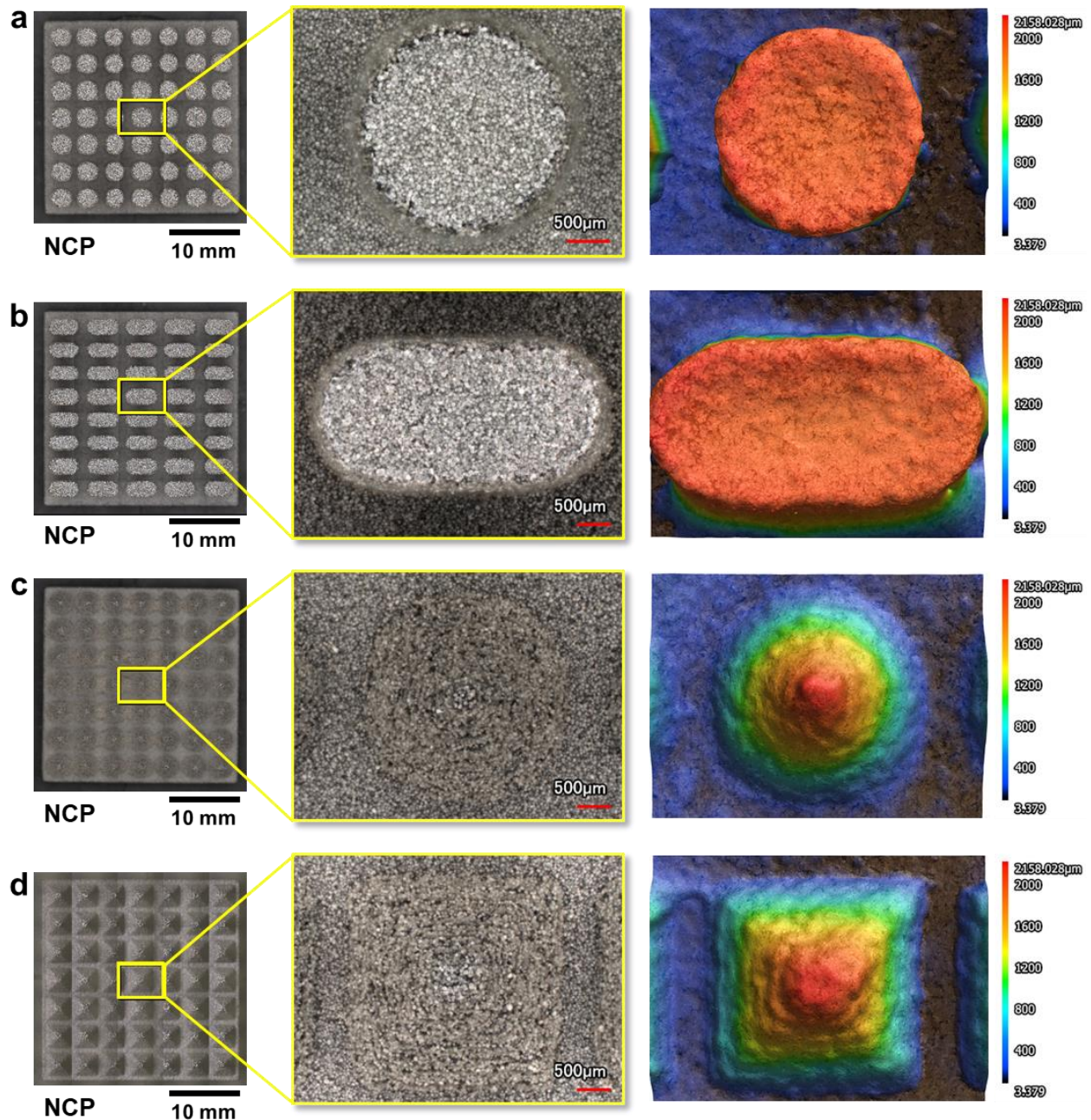


**Figure S9.** NCP images of the examined electrode architectures: (a) rod, (b) oval, (c) cone, and (d) pyramid patterns. The color maps correspond to height.

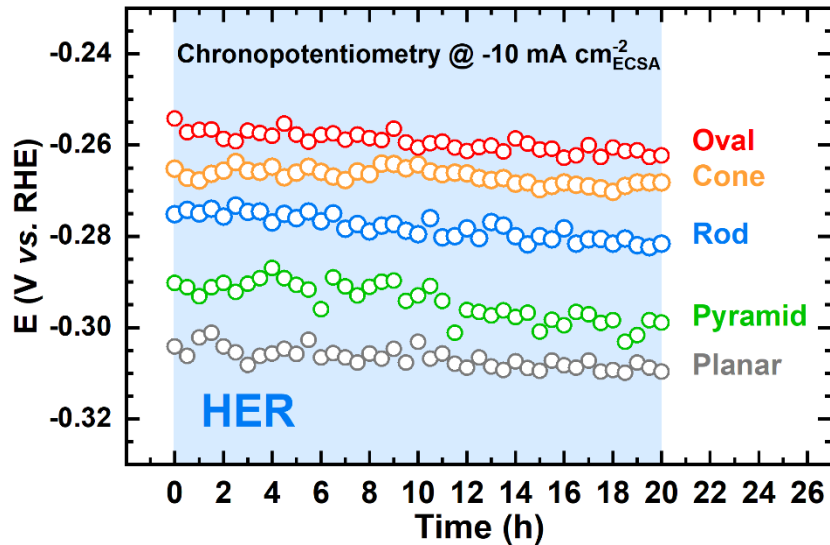


**Figure S10.** Chronopotentiometric tests at  $-10 \text{ mA cm}^{-2}$  for each electrode architecture.

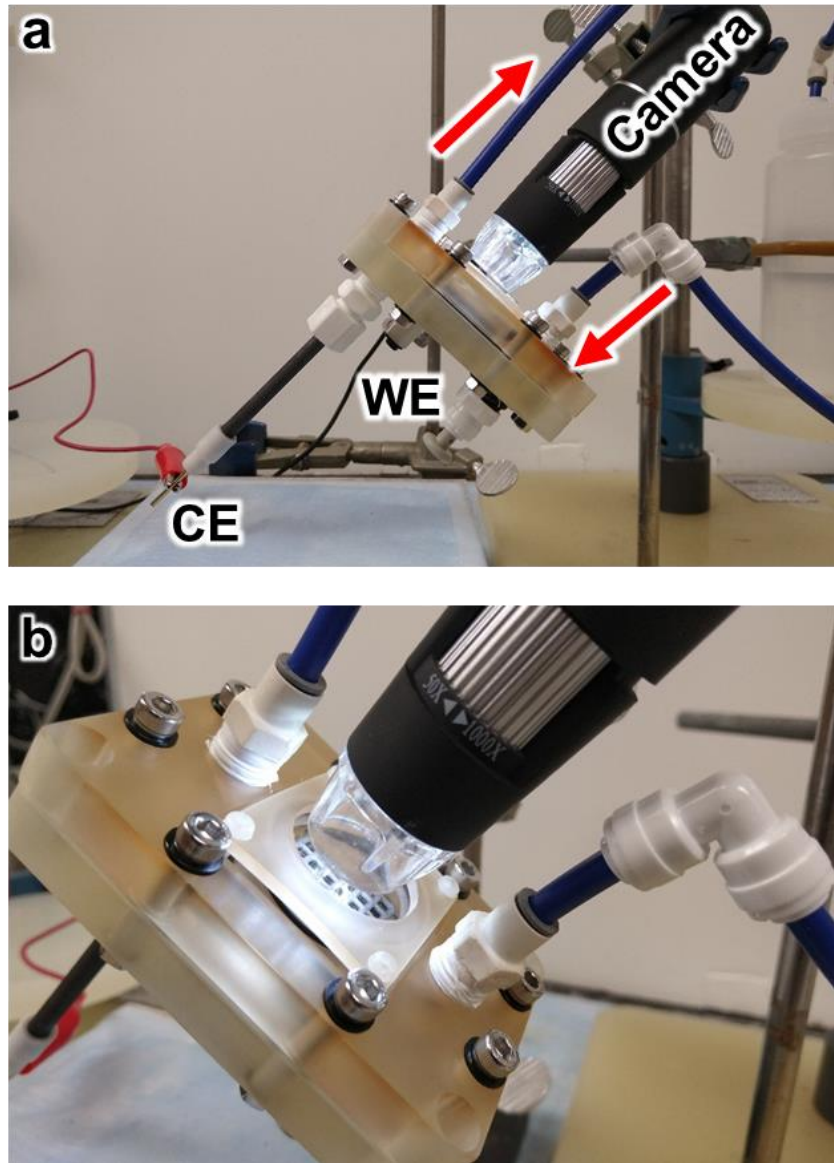


**Figure S11.** 3D-printed electrochemical flow cell utilized for bubble examination tests: (a) placement of the 3D-printed working electrode (WE) and graphite bar counter electrode (CE); arrows indicate the direction of flow. (b) Enlarged view showing the quartz window and the optical microscope positioned right above.

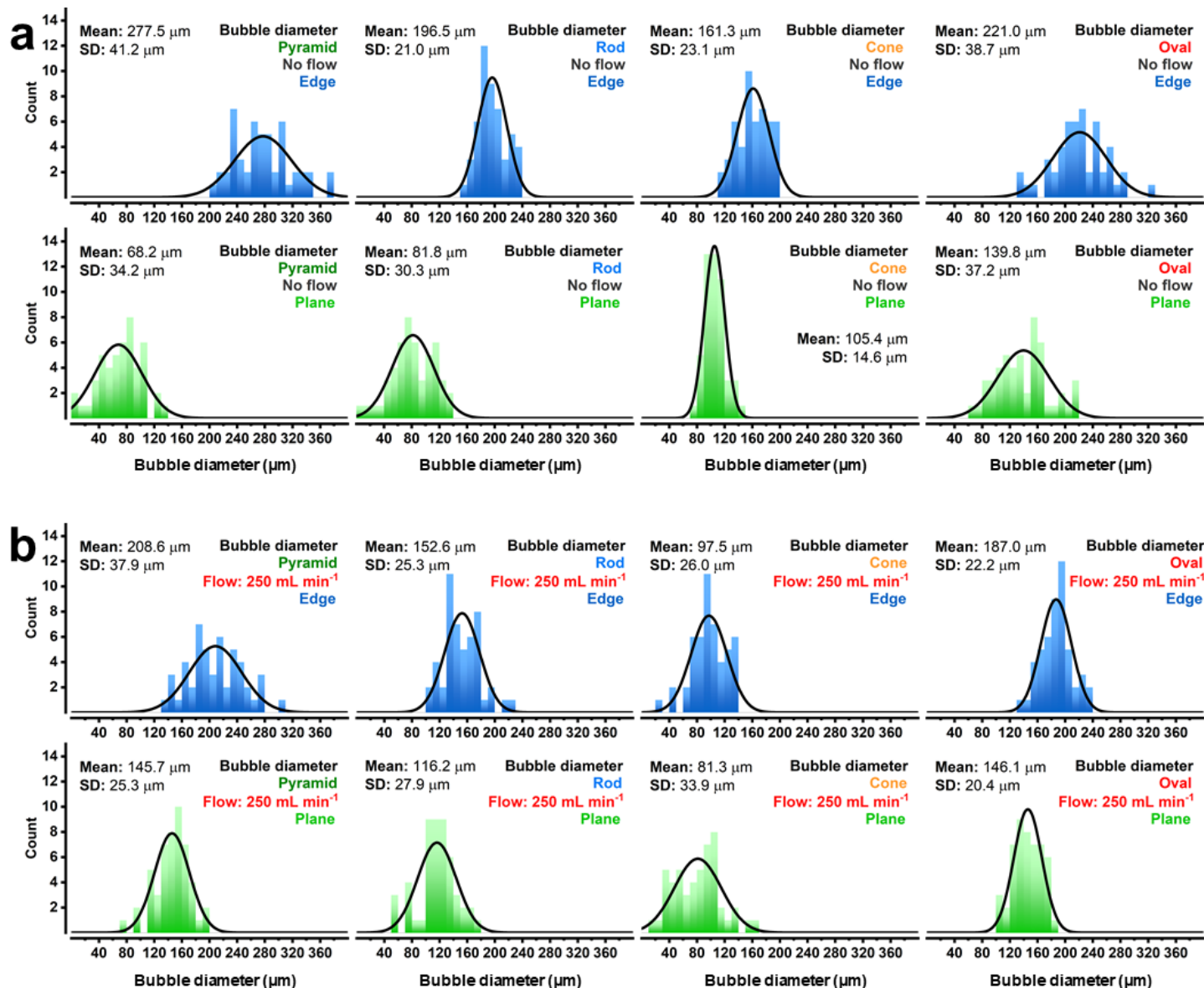
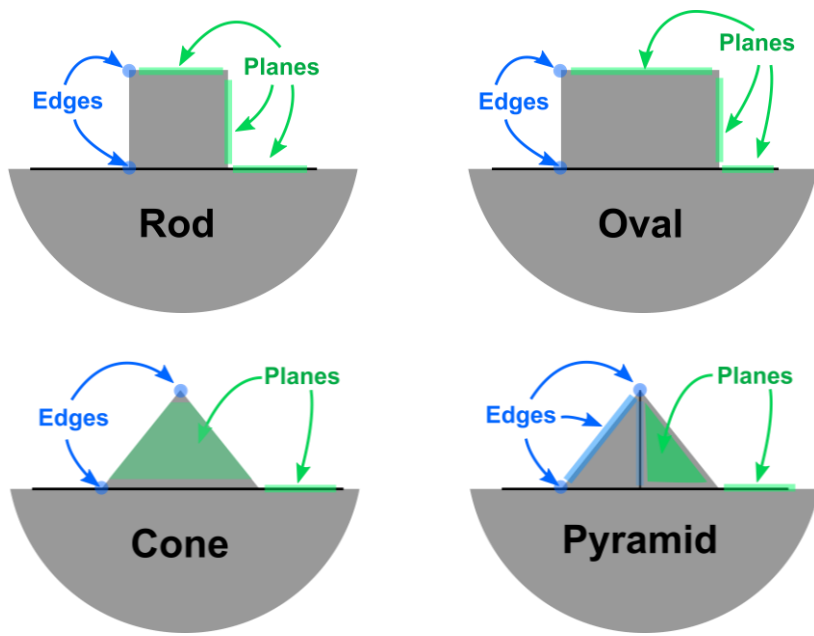


**Figure S12.** Histograms of bubble diameters at departure under (a) stagnant and (b) controlled flow conditions.



**Scheme S2.** Proposed classification of edge and plane sites for the studied geometries.

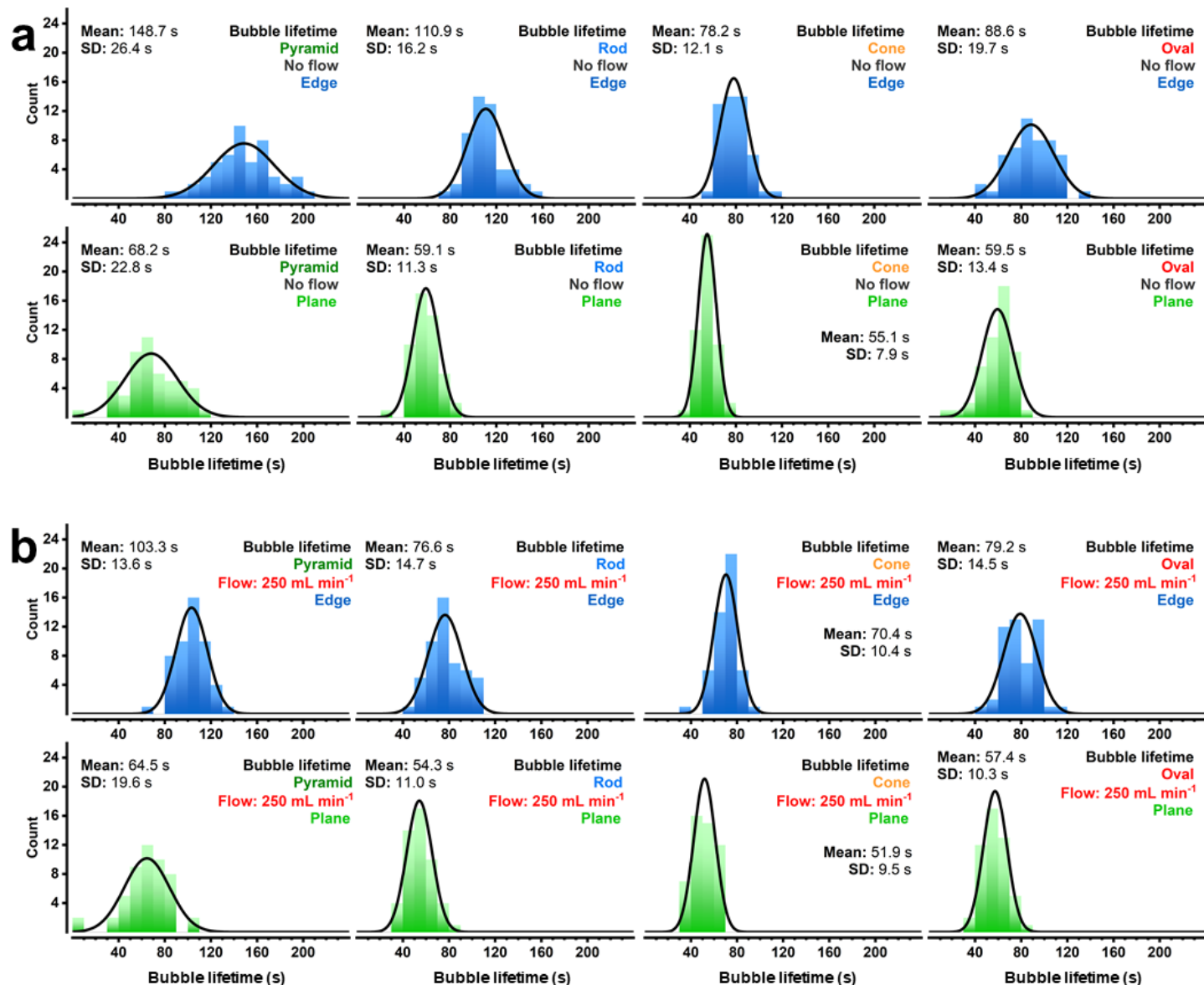


**Figure S13.** Histograms of bubble lifetimes under (a) stagnant and (b) controlled flow conditions.

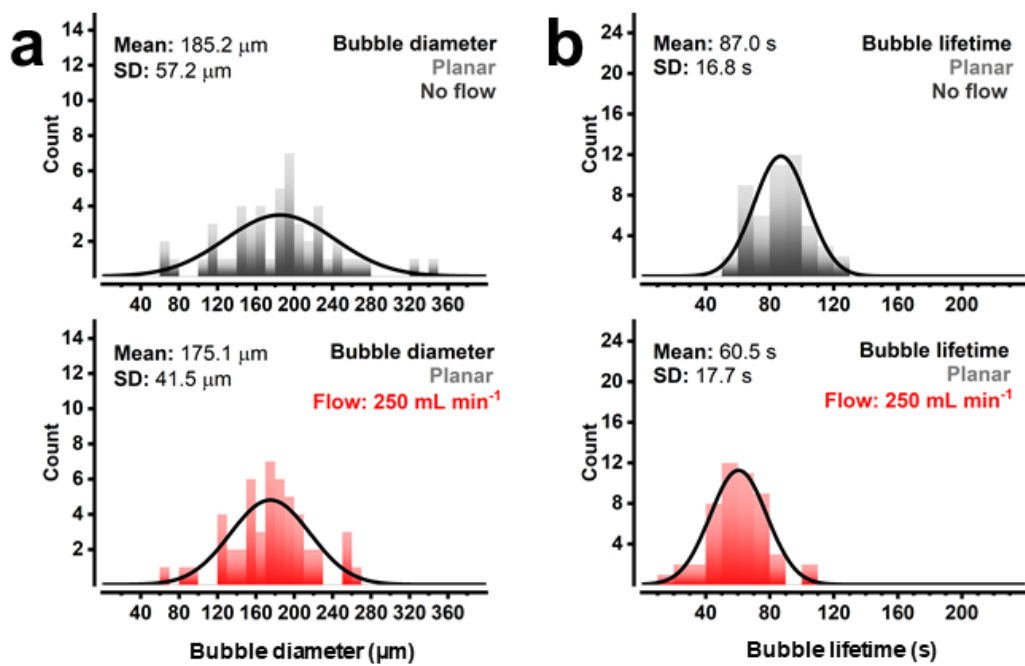


**Figure S14.** Histograms of (a) bubble diameters and (b) lifetimes for the planar electrode architecture under stagnant and controlled flow conditions.

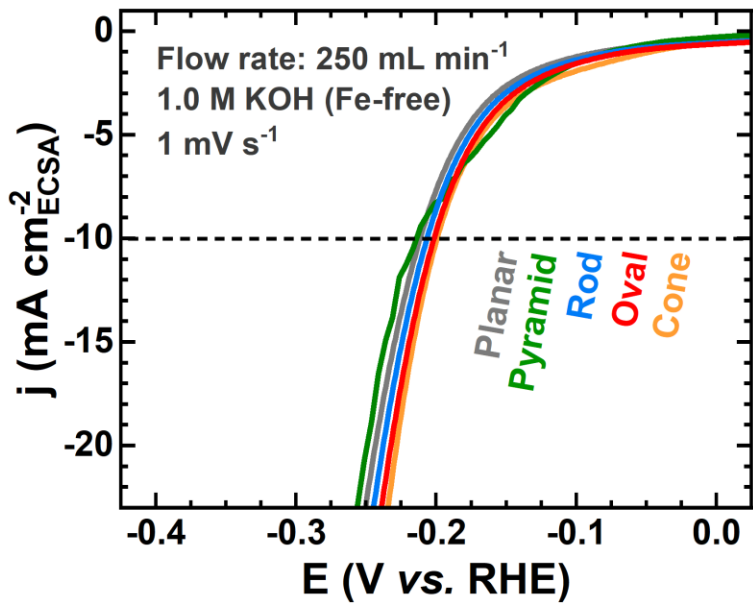


**Figure S15.** LSV scans in the HER region for each electrode architecture under forced-flow conditions ( $250 \text{ mL min}^{-1}$ ).

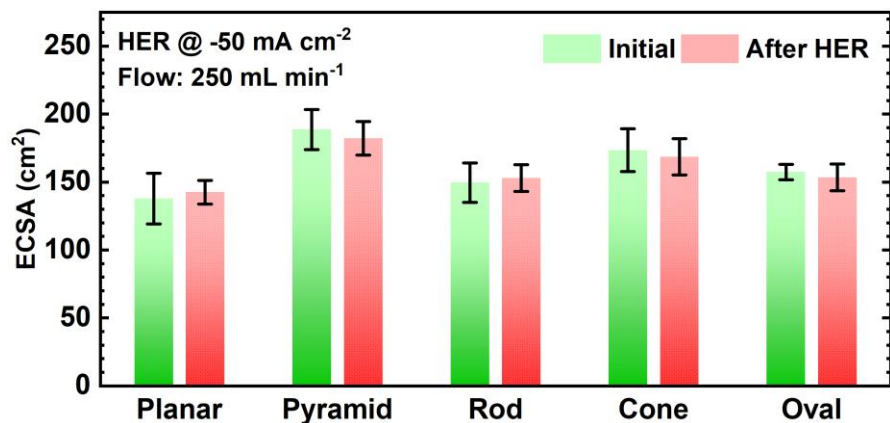


**Figure S16.** ECSA of the examined architectures during hydrogen bubble evolution tests. ECSA was estimated from double-layer capacitance measurements in the non-faradaic region, and calculated using a  $C_s$  of 40  $\mu\text{F}/\text{cm}^2$ .

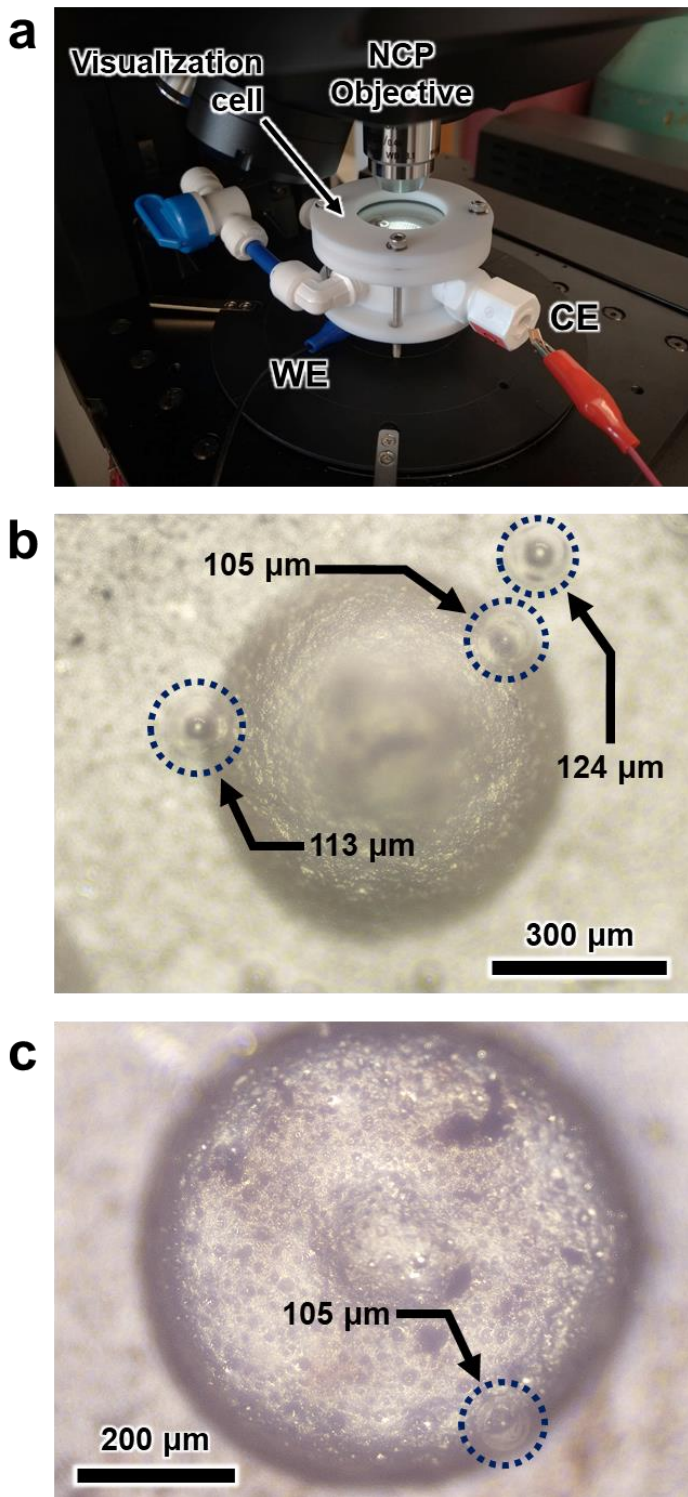


**Figure S17.** Electrode feature size effects on bubble size and lifetime during the HER: (a) photo of the PTFE visualization cell placed below a 20x objective of the optical profilometer; NCP images taken during bubble evolution on (b) cone and (c) rod-like features depicting isolated bubbles emerging from edges and planes.

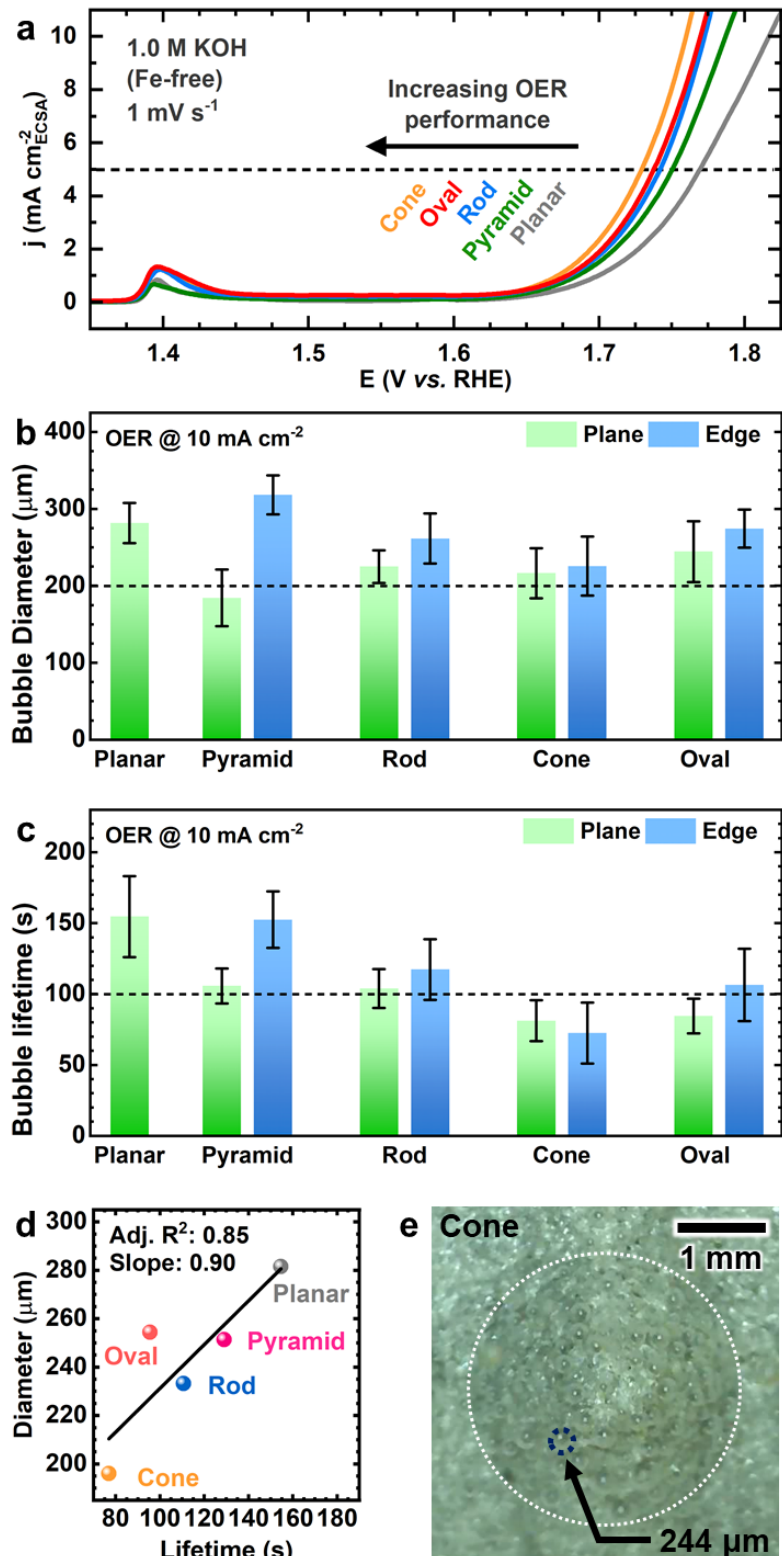


**Figure S18.** Electrode architecture effects on bubble size and lifetime during the OER: (a) LSV scans in OER region for each electrode architecture, (b) bubble diameters and (c) bubble lifetimes measured from edges and planes under stagnant conditions, (d) plot of bubble diameter vs. bubble lifetime, (e) NCP image of the cone shape during O<sub>2</sub> bubble evolution.

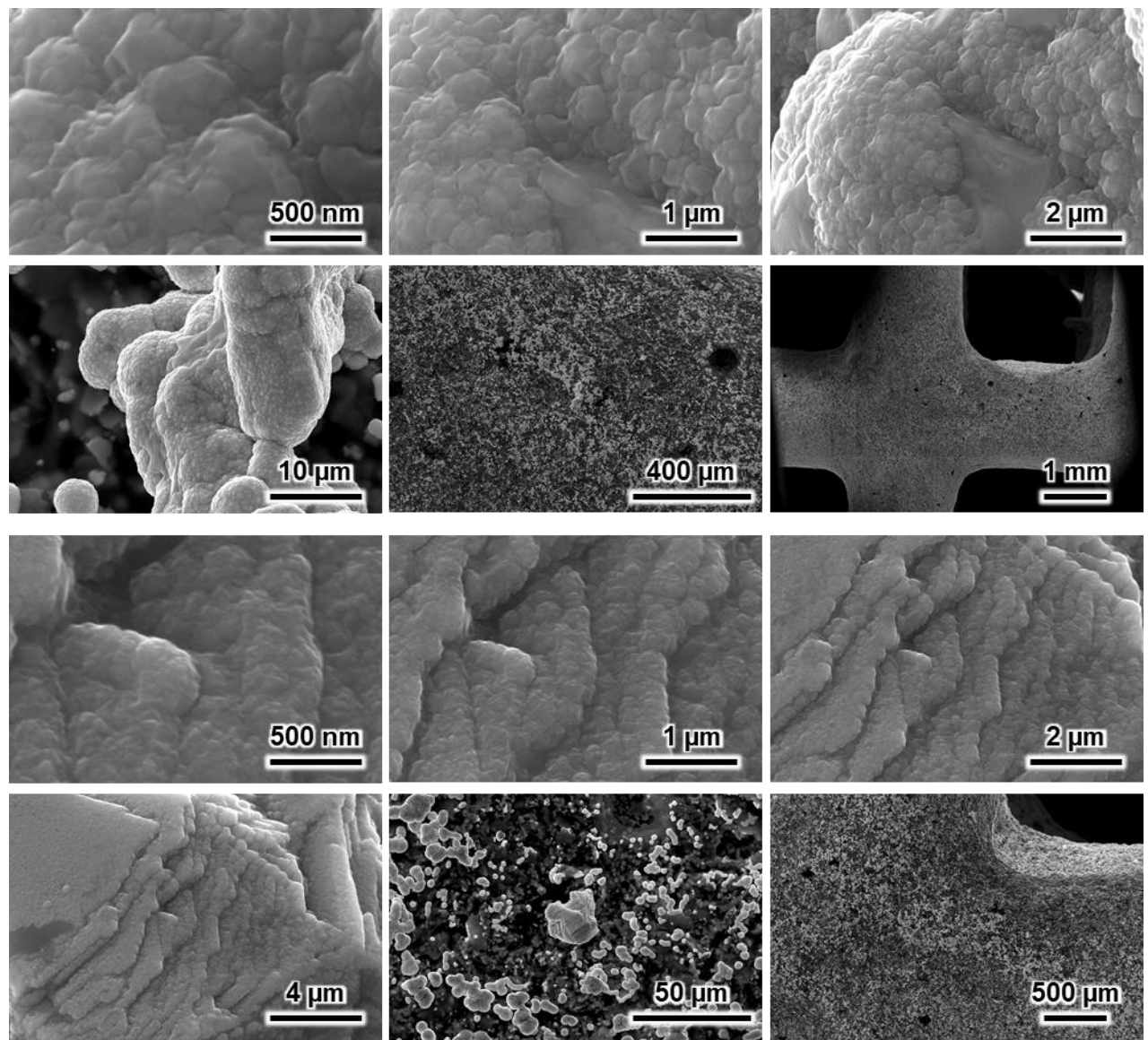


**Figure S19.** Additional SEM images of the Ni-coated 3D-printed porous electrode (3D-Ni/Cu).

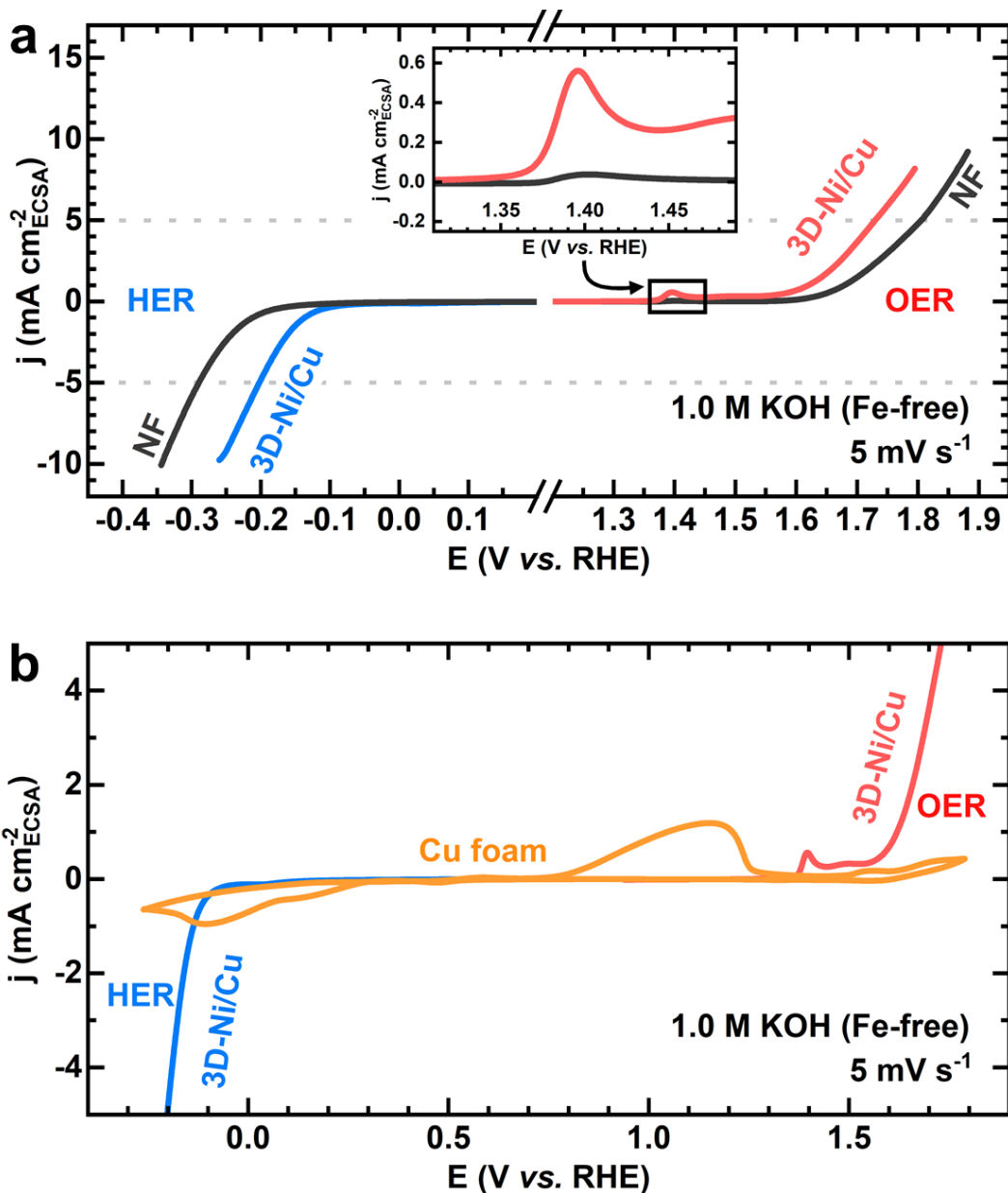


**Figure S20.** ECSA-normalized HER and OER polarization curves of the 3D-Ni/Cu porous electrode and control samples: (a) Ni foam and (b) Cu foam.  $\text{ECSA}_{\text{3D-Ni/Cu}}: 238.4 \text{ cm}^2$ ;  $\text{ECSA}_{\text{NF}}: 30.12 \text{ cm}^2$ ;  $\text{ECSA}_{\text{CF}}: 118.6 \text{ cm}^2$ .

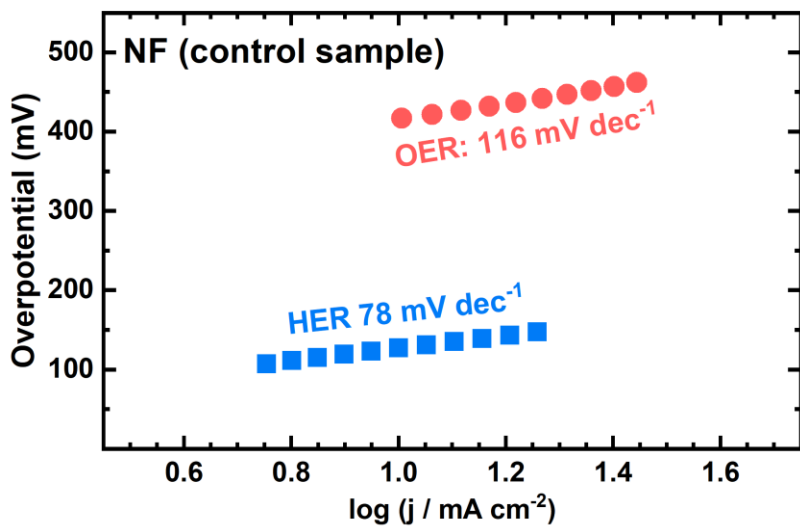


**Figure S21.** Tafel slopes for the NF control sample.

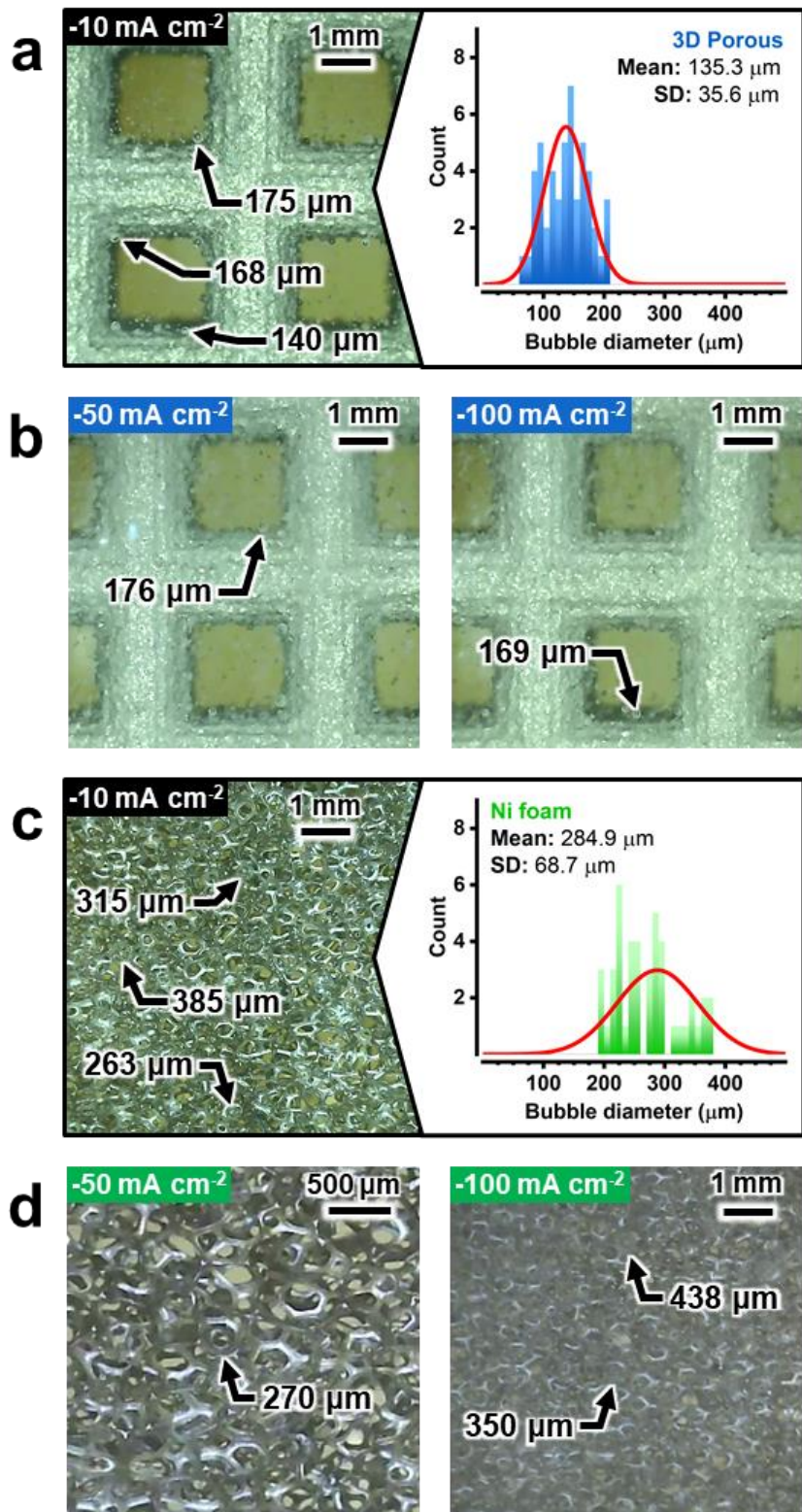


**Figure S22.** Bubble evolution of the 3D-Ni/Cu electrode: (a) NCP image and bubble size distribution at  $-10 \text{ mA}\cdot\text{cm}^{-2}$ , (b) bubble evolution snapshots at higher current densities. Bubble evolution of a NF control sample: (c) NCP image and bubble size distribution at  $-10 \text{ mA}\cdot\text{cm}^{-2}$ , (d) bubble evolution snapshots at higher current densities.

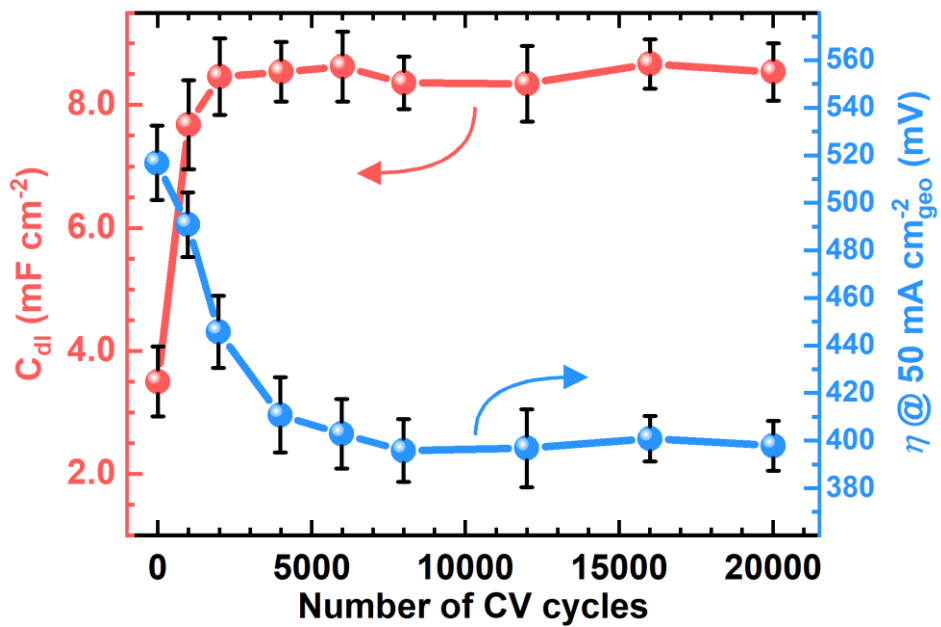


**Figure S23.** Double-layer capacitance (left axis) and activity (right axis) changes during CV cycling of the 3D-Ni/Cu electrode.

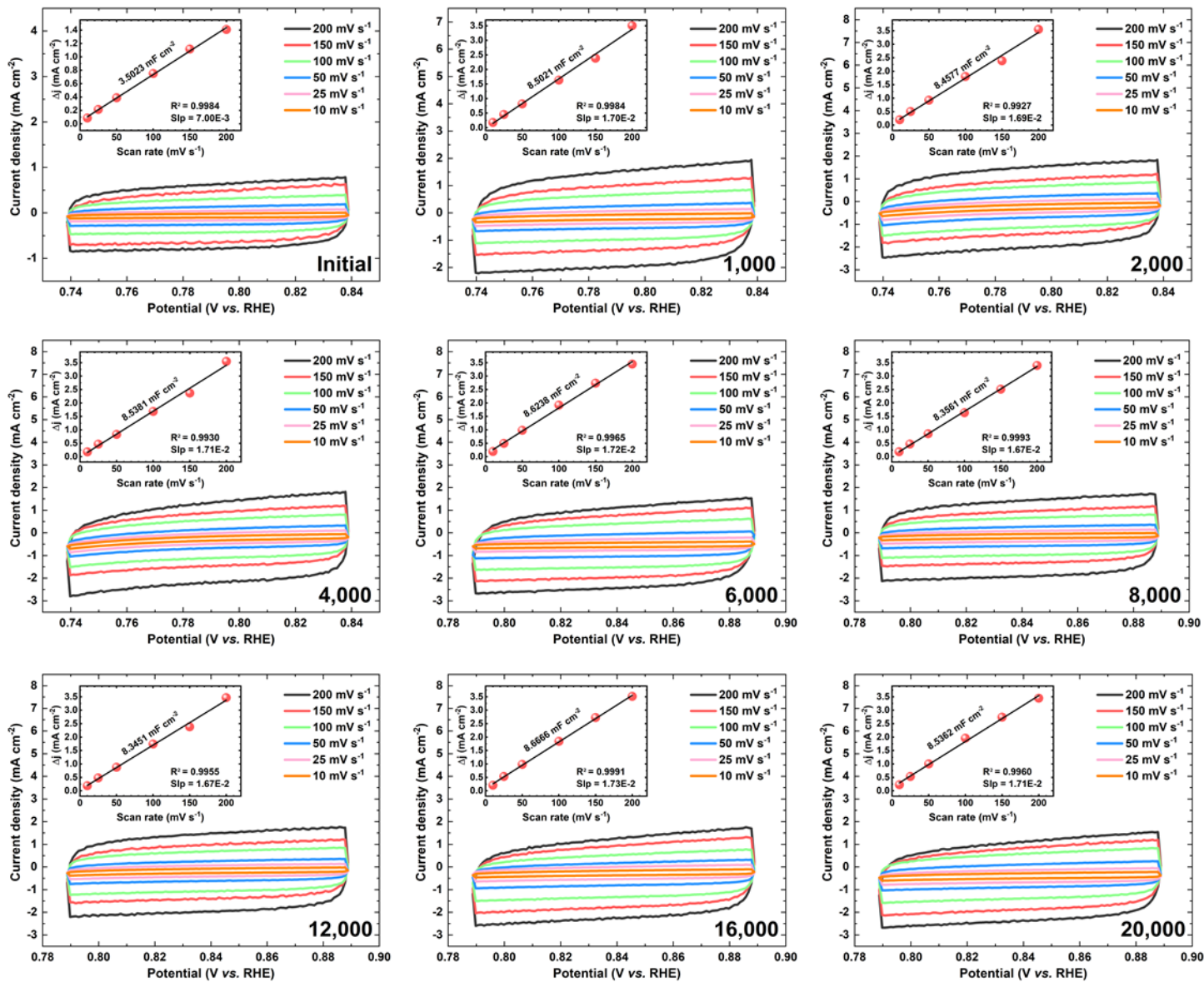


**Figure S24.** CV scans in the non-faradaic region for estimating the  $C_{dl}$  of 3D-Ni/Cu electrodes during OER cycling.

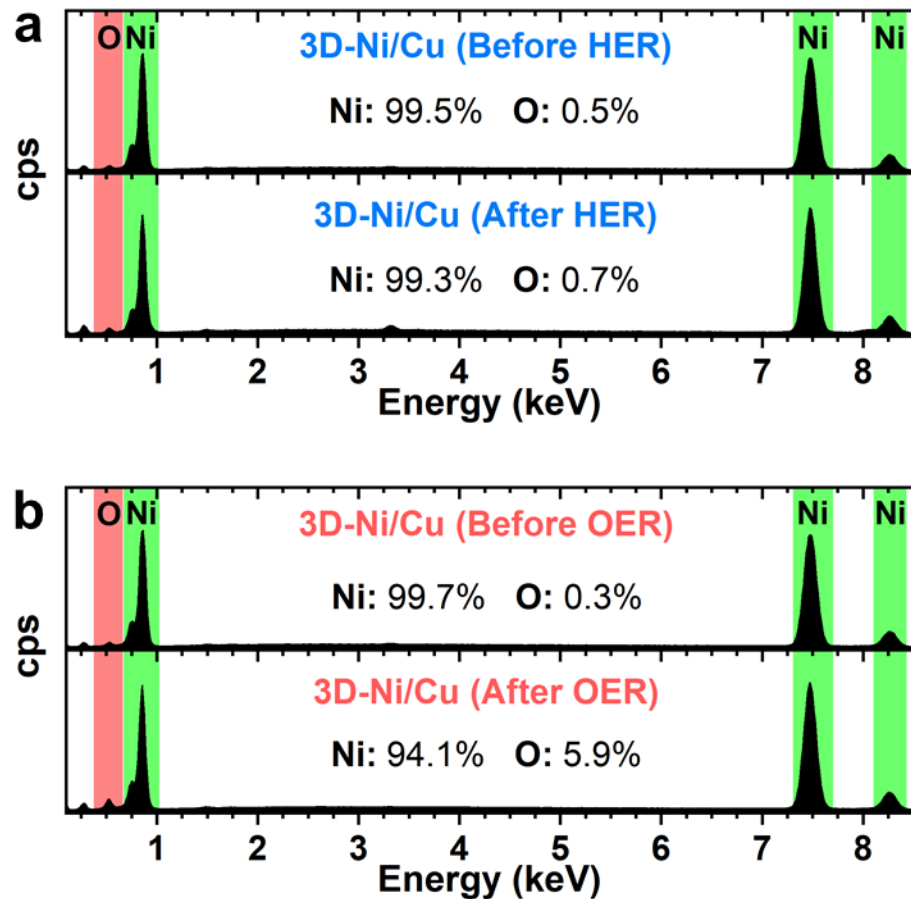


**Figure S25.** EDX spectra comparison before and after (a) HER and (b) OER tests using the 3D-Ni/Cu electrode.

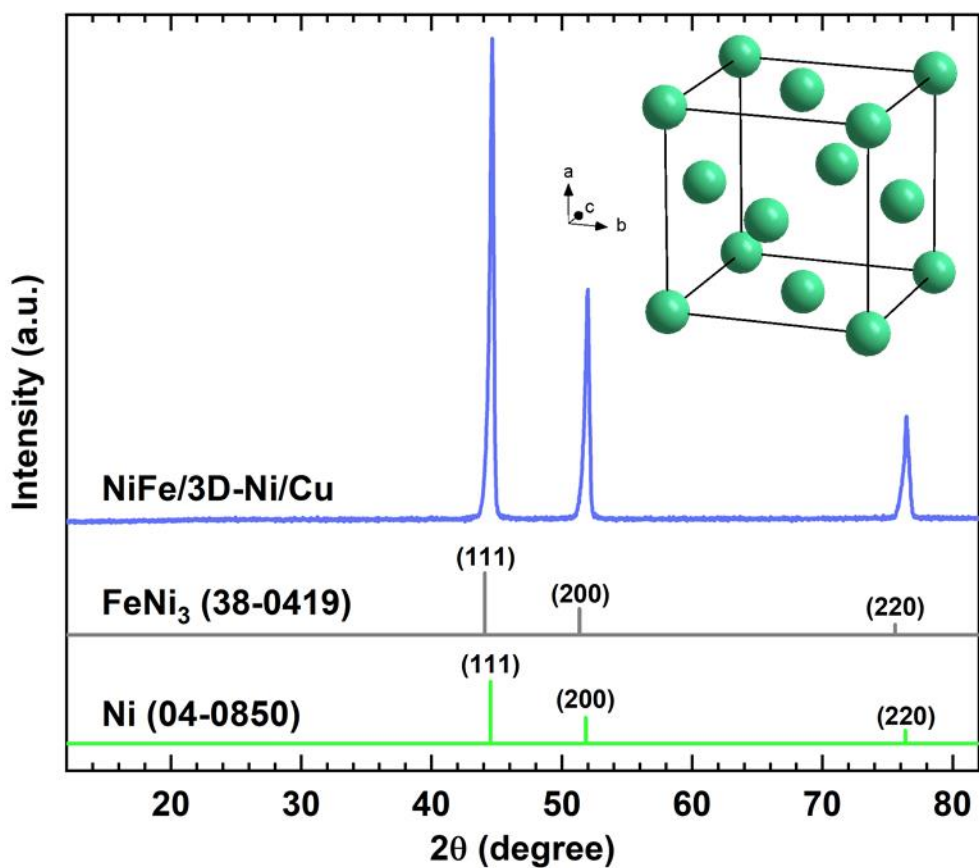


**Figure S26.** XRD pattern of the as-prepared NiFe/3D-Ni/Cu electrode. The inset shows the cubic  $\text{FeNi}_3$  structure.

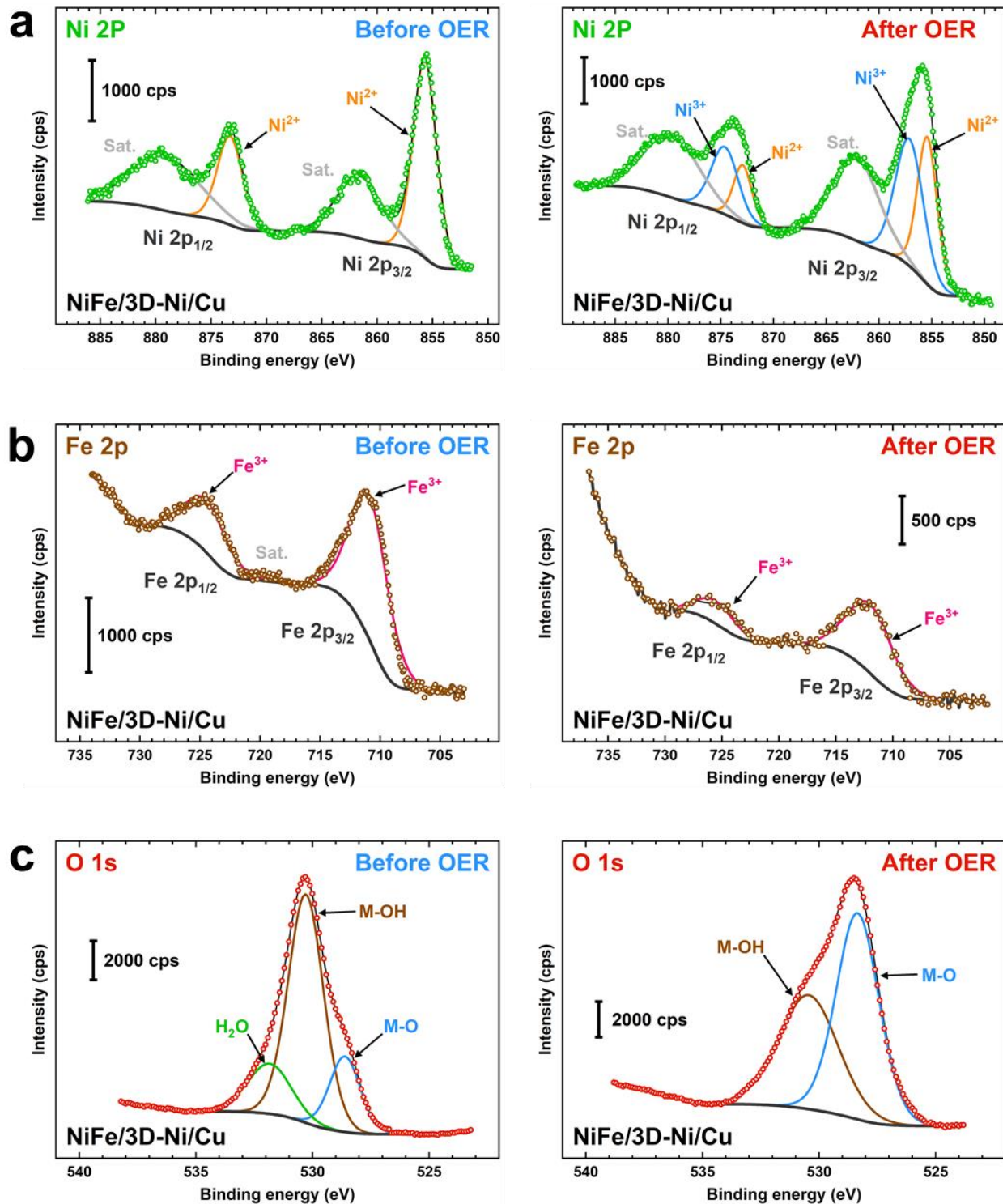


**Figure S27.** XPS spectra of the NiFe/3D-Ni/Cu electrode before and after OER cycling stability tests: (a) Ni 2p, (b) Fe 2p, and (c) O 1s peaks.

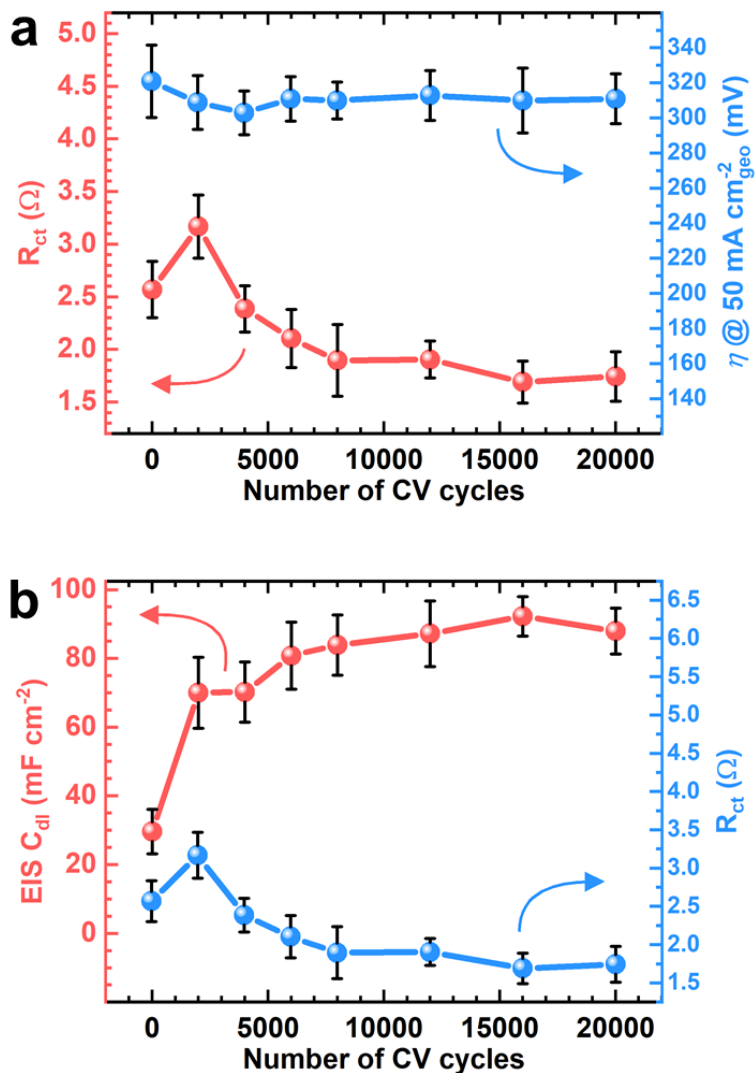


**Figure S28.** EIS measurements during OER cycling of the NiFe/3D-Ni/Cu electrode: (a) charge-transfer resistance and (b) double-layer capacitance (from EIS fitting using a Randles circuit).

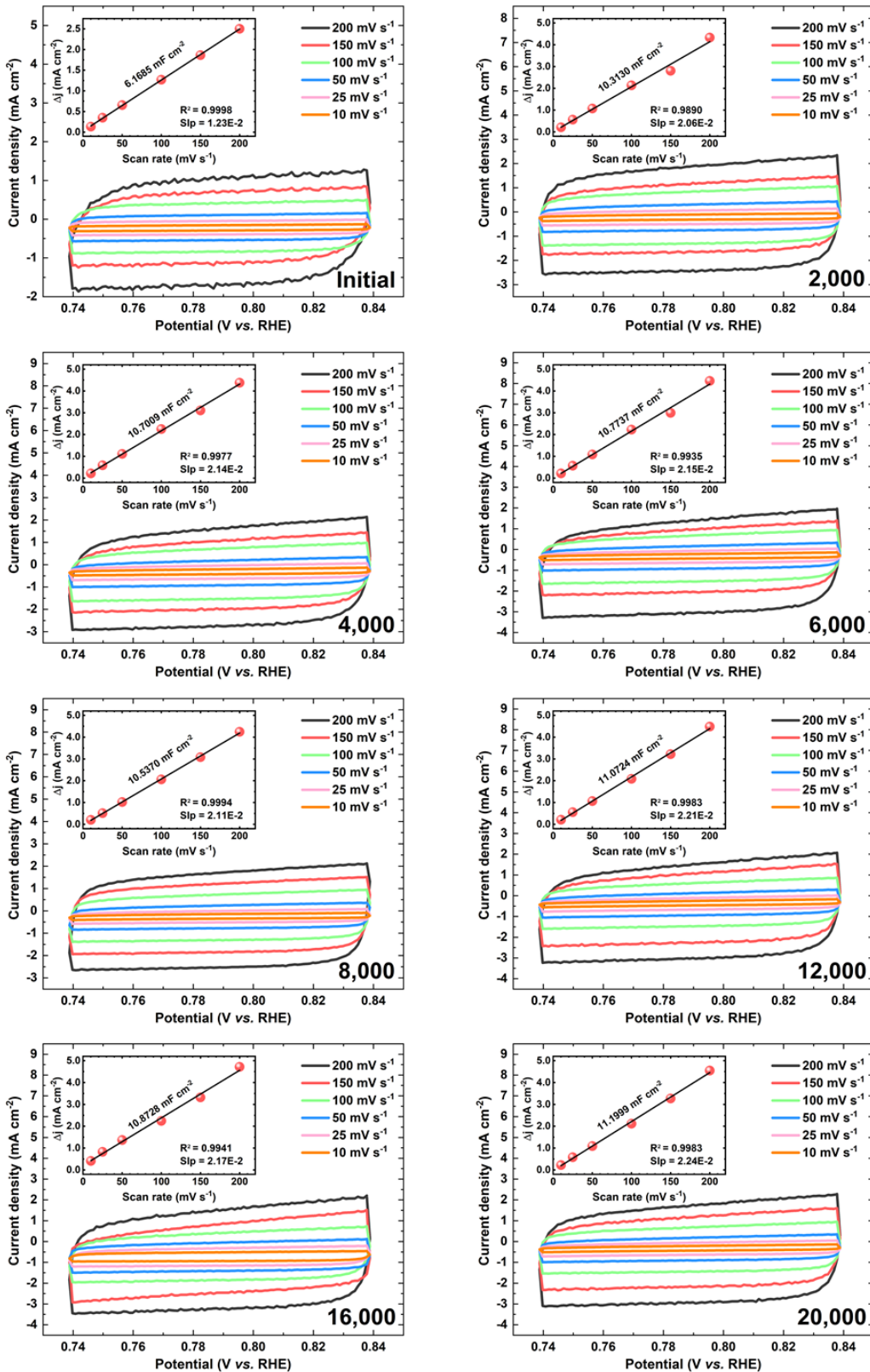


**Figure S29.** CV scans in the non-faradaic region for estimating the double-layer capacitance during OER cycling of the NiFe/3D-Ni/Cu electrode.

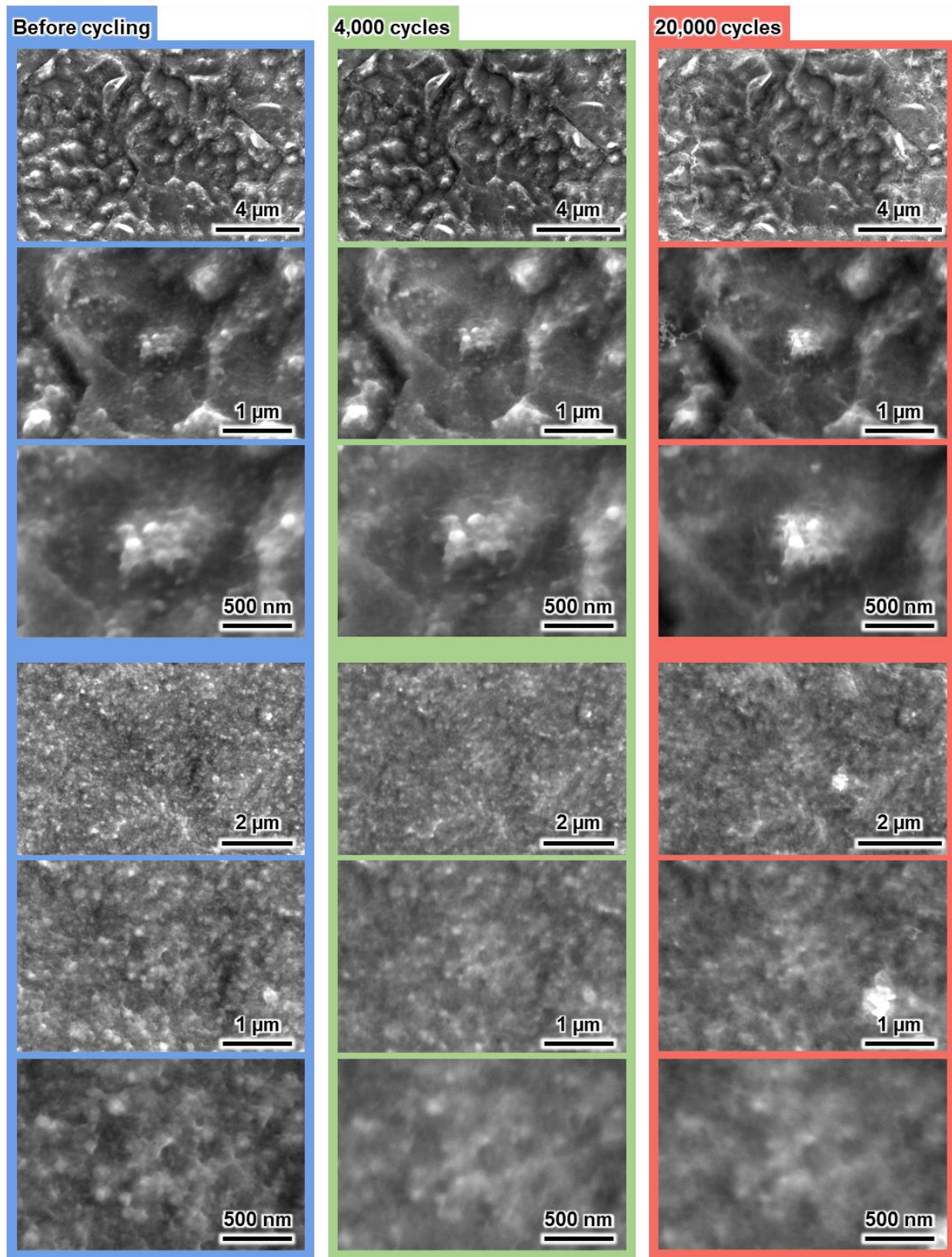


**Figure S30.** Additional SEM images of the NiFe/3D-Ni/Cu electrode during OER cycling.

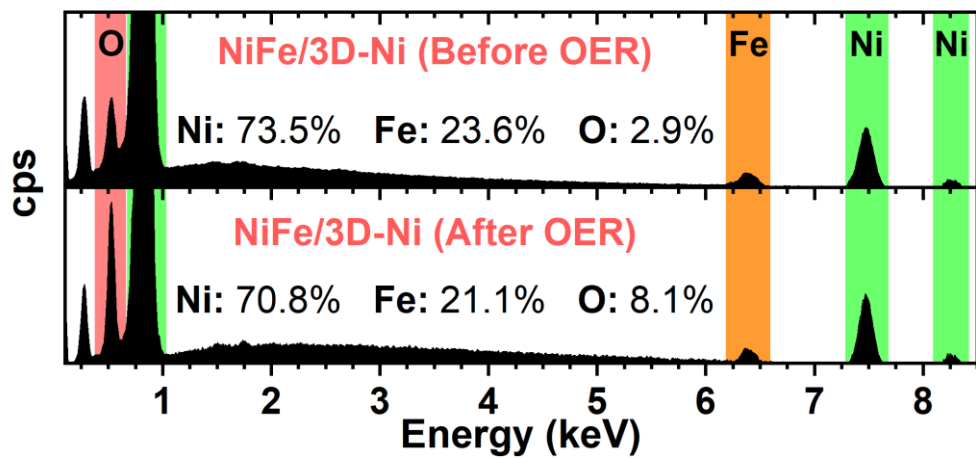


**Figure S31.** EDX spectra and elemental compositions of the NiFe/3D-Ni/Cu electrode before and after OER cycling.

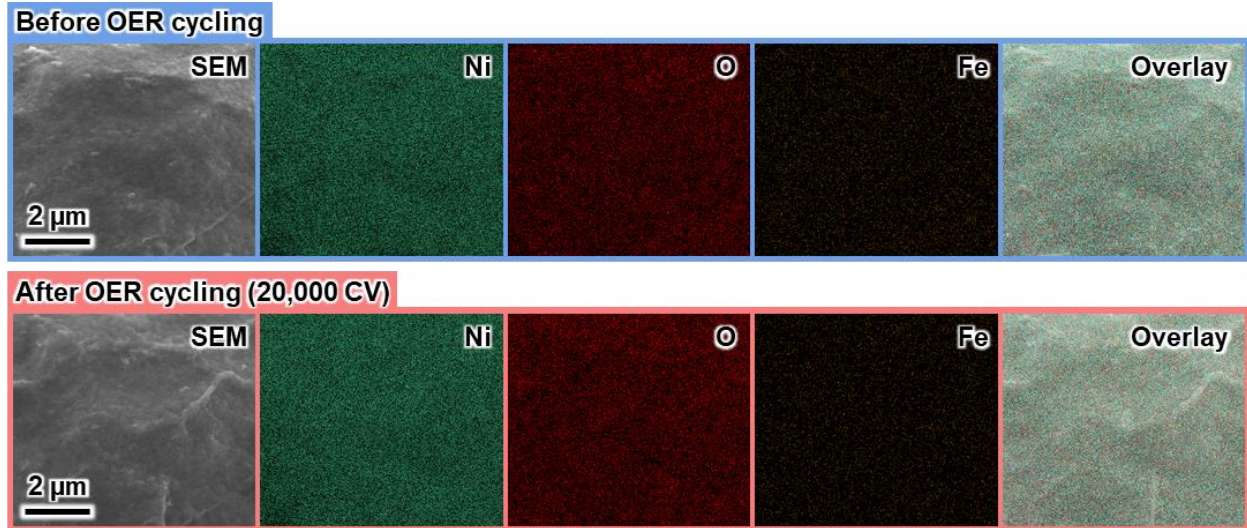


**Figure S32.** EDX elemental mappings of the NiFe/3D-Ni/Cu electrode surface before and after OER cycling.

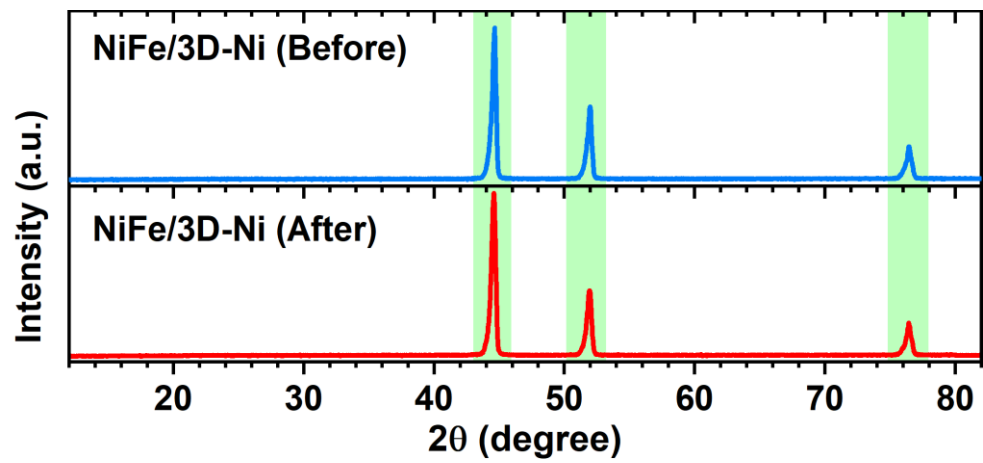
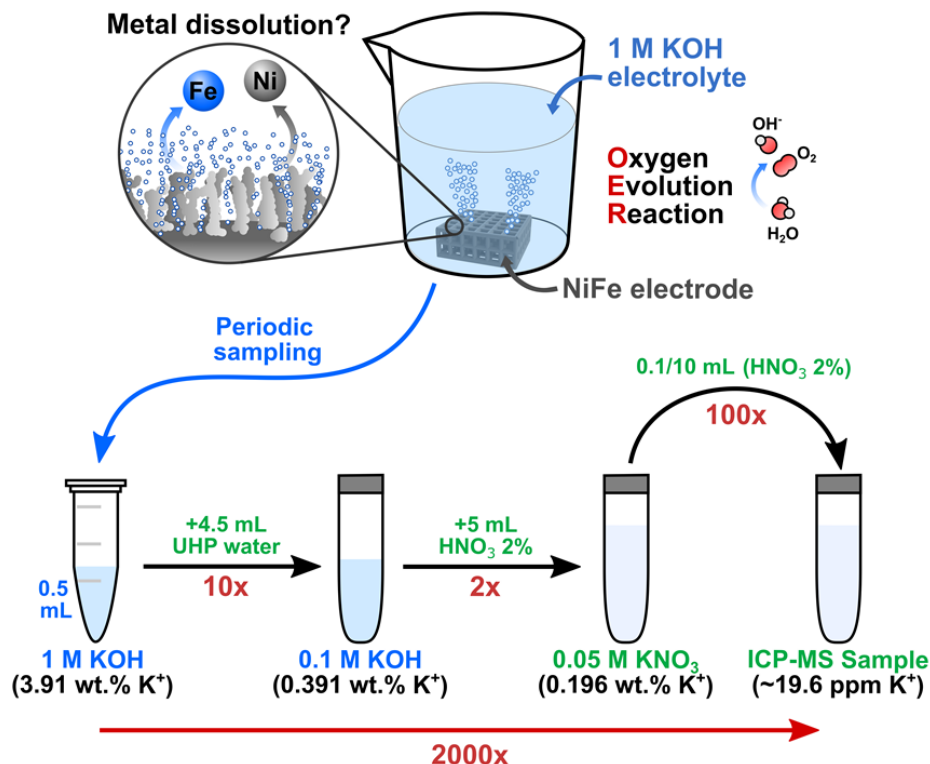


**Figure S33.** XRD patterns of the NiFe/3D-Ni/Cu electrode before and after OER cycling.

### Analysis of KOH electrolytes during OER cycling using ICP-MS

We probed the KOH electrolyte during stability tests using ICP-MS to detect any metal compositions that could be related to dissolution or incorporation processes. With the support of Dr. Nathaniel R. Miller, we developed an ICP-MS analytical method for examining concentrated KOH electrolytes. Based on previous approaches for analyzing KOH electrolyte,<sup>4,5</sup> we devised a procedure to dilute periodic electrolyte samples with ultra-high purity water and nitric acid, as depicted in **Scheme S3**.



**Scheme S3.** Dilution procedure utilized for electrolyte testing *via* solution-mode ICP-MS.

We optimized the instrument by tuning the plasma in no gas, He and H<sub>2</sub> modes. We also examined the accuracy and precision of the method by analyzing quality control and spiked samples, and obtained calibration curves for fifteen different isotopes (**Figure S29**). The complete analytical procedure, quality control results, and NiFe dissolution/incorporation results are detailed in the following website from the Jackson School of Geosciences, UT Austin:

<https://www.jsg.utexas.edu/geo392-f21-class-project-group-vf50otr6gr/>

## Analytes of interest

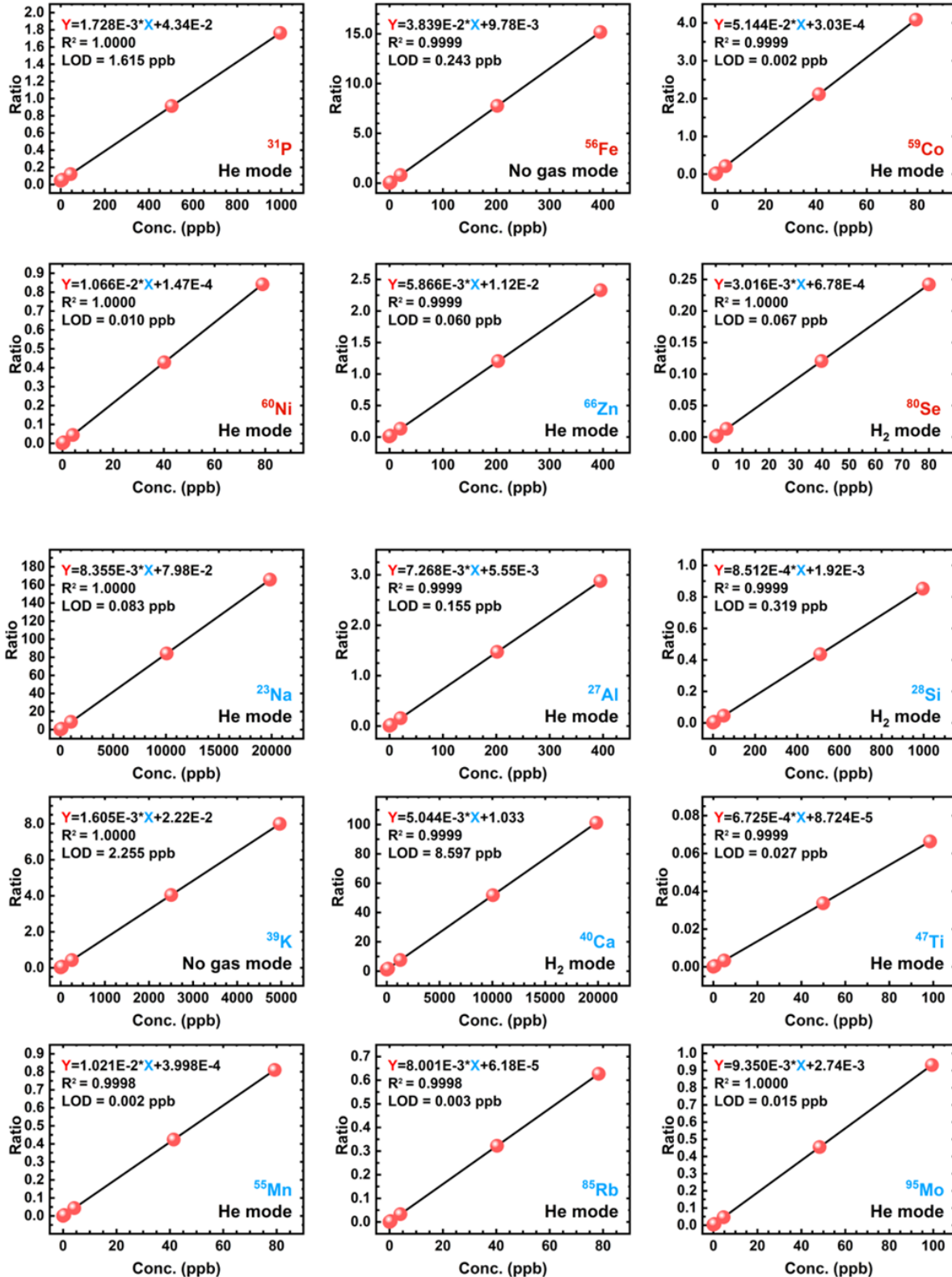


**Figure S34.** Calibration curves of the analytes studied using our ICP-MS method. Analytes of interest are shown in red, additional analytes (*i.e.*, electrolyte ions and potential glassware impurities) are shown in light blue.

**Table S3.** Concentrations (in ppb) of different analytes in purified KOH electrolyte obtained through solution mode ICP-MS.

Rep.	<sup>56</sup> Fe [#1]	<sup>59</sup> Co [#3]	<sup>60</sup> Ni [#3]
1	BDL	BDL	13.70
2	BDL	3.20	13.64
3	BDL	BDL	29.61
<b>Mean</b>	<b>n/a</b>	<b>n/a</b>	<b>13.98</b>
<b>SD</b>	n/a	n/a	0.54
<b>%RSD</b>	n/a	n/a	3.9

Rep.	<sup>23</sup> Na [#3]	<sup>27</sup> Al [#3]	<sup>28</sup> Si [#2]	<sup>39</sup> K [#1]	<sup>40</sup> Ca [#2]	<sup>47</sup> Ti [#3]	<sup>55</sup> Mn [#3]	<sup>66</sup> Zn [#3]	<sup>85</sup> Rb [#3]	<sup>95</sup> Mo [#3]
1	109954	344.8	458788	37607877	BDL	BDL	4.99	BDL	3227	1043
2	107579	716.5	414774	37224360	BDL	BDL	6.45	BDL	3327	420
3	105269	71.2	411521	37538788	BDL	BDL	4.70	BDL	3465	BDL
<b>Mean</b>	<b>107601</b>	<b>377.5</b>	<b>428361</b>	<b>37457008</b>	<b>n/a</b>	<b>n/a</b>	<b>5.38</b>	<b>n/a</b>	<b>3339</b>	<b>732</b>
<b>SD</b>	2342	323.9	26401	204419	n/a	n/a	0.94	n/a	120	441
<b>%RSD</b>	2.2	85.8	6.2	0.5	n/a	n/a	17.4	n/a	3.6	60.3

**Note:** Collision reaction cell modes are represented as follows: #1: no gas mode, #2: H<sub>2</sub> mode, #3: He mode. BDL: below detection limit, SD: standard deviation, RSD: relative standard deviation.

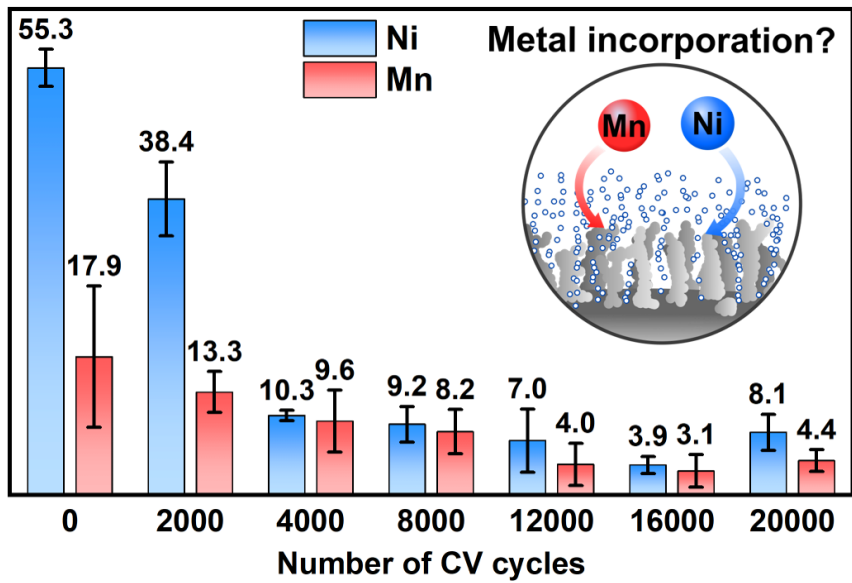
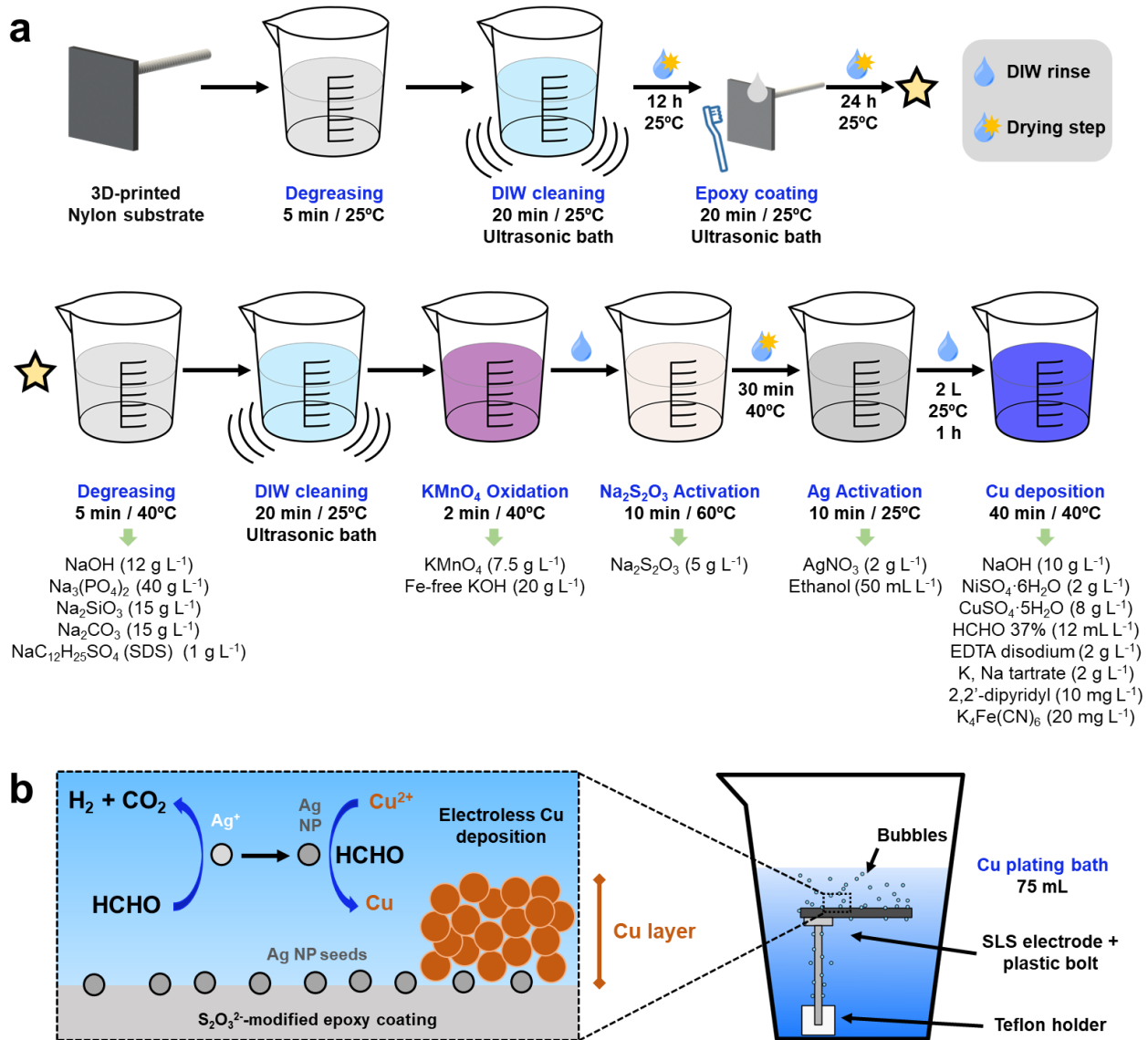


**Figure S35.** Concentrations (in ppb) of Ni and Mn ions in Fe-free KOH electrolyte during OER cycling of the NiFe/3D-Ni/Cu electrode. The inset depicts the suspected metal re-incorporation process based on the Ni, Mn concentration decrease during OER stability tests.



**Scheme S4.** Electroless Cu deposition process: (a) experimental workflow for depositing Cu on epoxy-coated Nylon substrates and (b) schematic illustration of the experimental Cu bath and the chemical processes occurring during electroless deposition. DIW: deionized water.

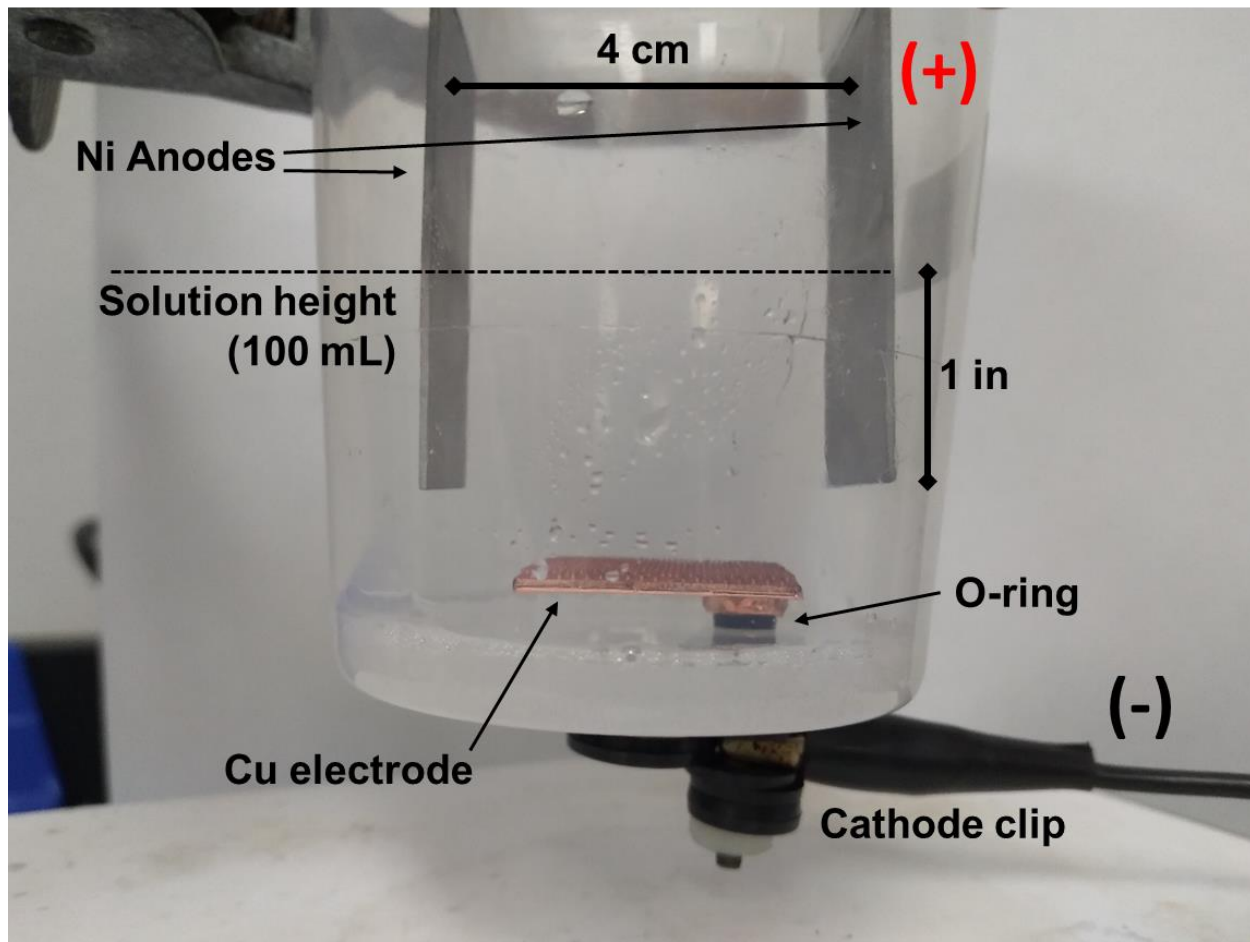
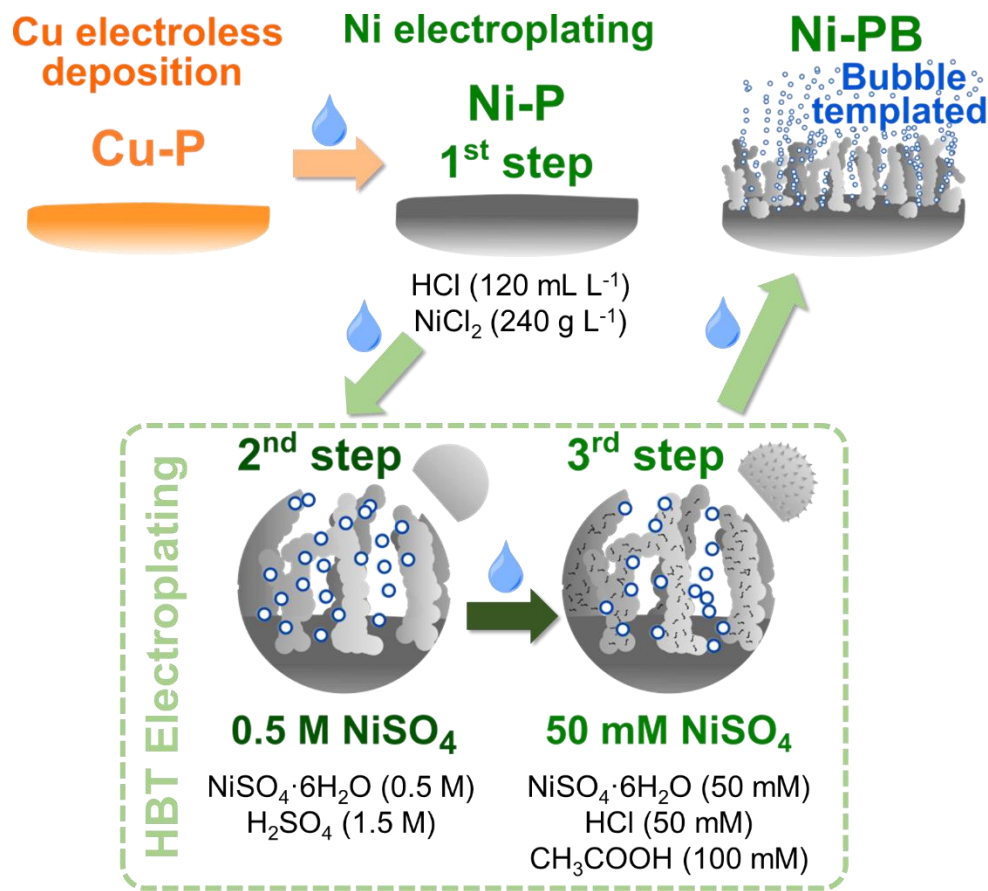
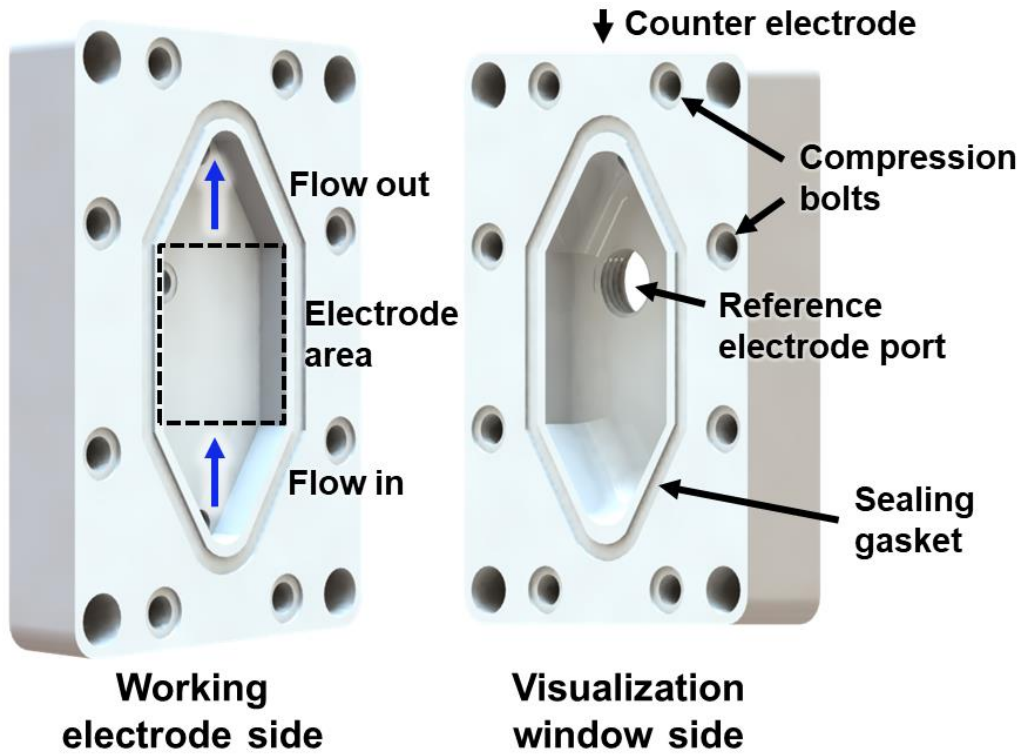


**Figure S36.** Custom electrochemical cell utilized during Ni electrodeposition steps.



**Scheme S5.** Ni electrodeposition procedure including Ni plating bath compositions.



**Scheme S6.** Custom 3D-printed electrochemical flow cell utilized during OER performance tests. Cell frames were made using stereolithography 3D printing with clear resin. Suitable metal-free plastic connections (for reverse osmosis) were utilized as electrode ports and flow inlet/outlets.

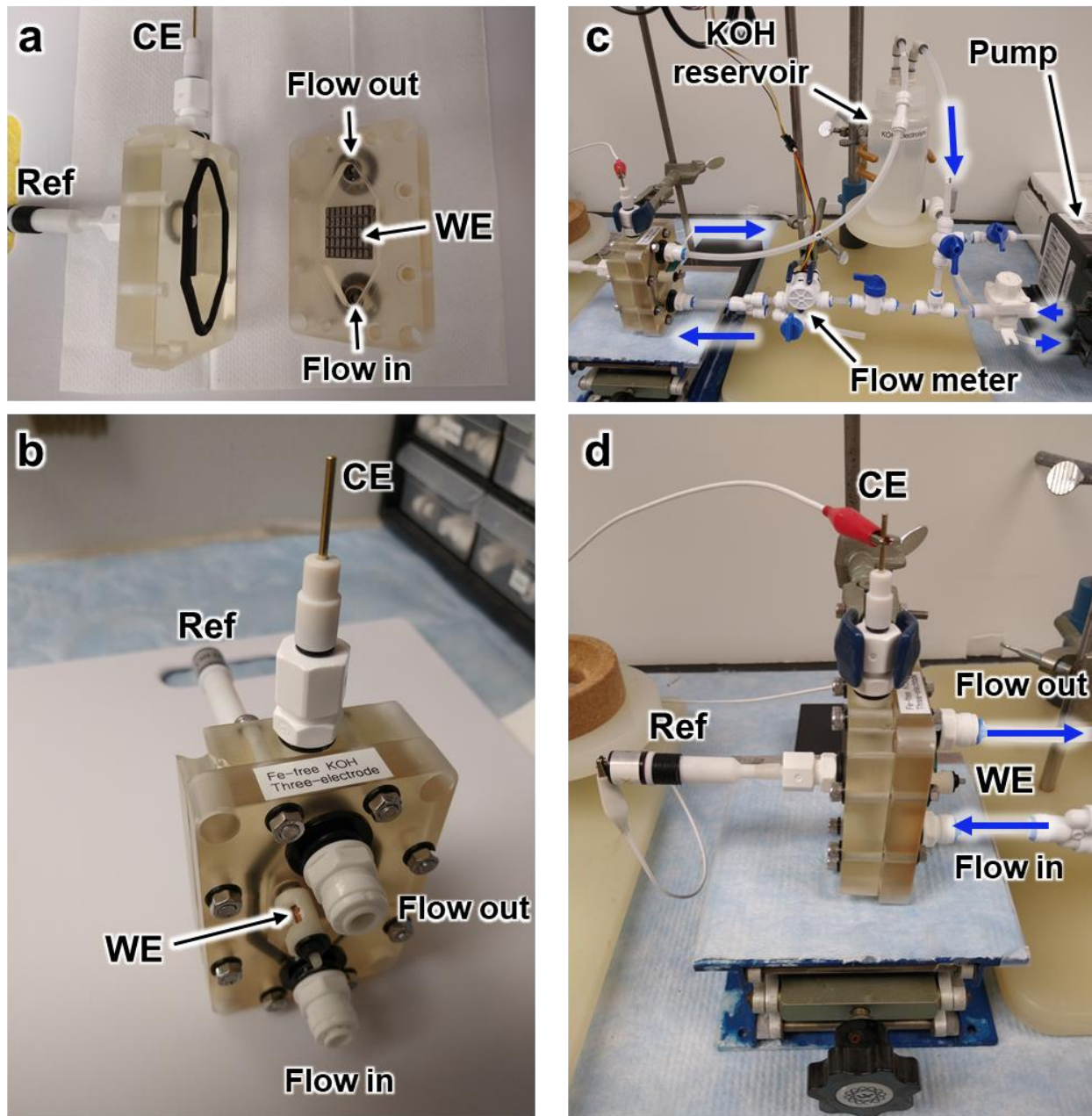


**Figure S37.** Pictures of the custom 3D-printed electrochemical flow cell utilized during OER performance tests: (a) disassembled cell, (b) flow circuit components, (c) assembled cell, and (d) side view of the assembled cell connected to the flow circuit. Reference electrode (Ref): Hg/HgO in Fe-free 1.0 M KOH. Counter electrode (CE): graphite rode. Flow configuration adapted from our previous studies (Refs. <sup>6-9</sup>).

## References

- (1) Biesinger, M. C. Advanced Analysis of Copper X-Ray Photoelectron Spectra. *Surf. Interface Anal.* **2017**, *49* (13), 1325–1334. <https://doi.org/10.1002/sia.6239>.
- (2) Goh, S. W.; Buckley, A. N.; Lamb, R. N.; Rosenberg, R. A.; Moran, D. The Oxidation States of Copper and Iron in Mineral Sulfides, and the Oxides Formed on Initial Exposure of Chalcopyrite and Bornite to Air. *Geochimica et Cosmochimica Acta* **2006**, *70* (9), 2210–2228. <https://doi.org/10.1016/j.gca.2006.02.007>.
- (3) Wang, Y.; Ni, L.; Yang, F.; Gu, F.; Liang, K.; Marcus, K.; Wan, Y.; Chen, J.; Feng, Z. Facile Preparation of a High-Quality Copper Layer on Epoxy Resin via Electroless Plating for Applications in Electromagnetic Interference Shielding. *J. Mater. Chem. C* **2017**, *5* (48), 12769–12776. <https://doi.org/10.1039/C7TC03823B>.
- (4) Patidar, R.; Rebari, B.; Bhadu, G. R.; Patel, G. ICP-MS Method Development and Validation for Determination of Trace Elemental Impurities in Caustic Potash. *International Journal of Mass Spectrometry* **2020**, *454*, 116356. <https://doi.org/10.1016/j.ijms.2020.116356>.
- (5) Lu, Y.; Sun, Y. An On-Line Electrodialyzer-ICP-MS Analytical System for Direct Determination of Trace Metal Impurities in KOH. *J. Anal. At. Spectrom.* **2008**, *23* (4), 574–578. <https://doi.org/10.1039/B712296A>.
- (6) Marquez-Montes, R. A.; Kawashima, K.; Son, Y. J.; Weeks, J. A.; Sun, H. H.; Celio, H.; Ramos-Sánchez, V. H.; Mullins, C. B. Mass Transport-Enhanced Electrodeposition of Ni–S–P–O Films on Nickel Foam for Electrochemical Water Splitting. *J. Mater. Chem. A* **2021**, *9*, 7736–7749. <https://doi.org/10.1039/D0TA12097A>.
- (7) Kawashima, K.; Márquez-Montes, R. A.; Li, H.; Shin, K.; Cao, C. L.; Vo, K. M.; Son, Y. J.; Wygant, B. R.; Chunangad, A.; Youn, D. H.; Henkelman, G.; Ramos-Sánchez, V. H.; Mullins, C. B. Electrochemical Behavior of a Ni<sub>3</sub>N OER Precatalyst in Fe-Purified Alkaline Media: The Impact of Self-Oxidation and Fe Incorporation. *Mater. Adv.* **2021**. <https://doi.org/10.1039/D1MA00130B>.
- (8) Márquez-Montes, R. A.; Collins-Martínez, V. H.; Pérez-Reyes, I.; Chávez-Flores, D.; Graeve, O. A.; Ramos-Sánchez, V. H. Electrochemical Engineering Assessment of a Novel 3D-Printed Filter-Press Electrochemical Reactor for Multipurpose Laboratory Applications. *ACS Sustain. Chem. Eng.* **2020**, *8* (9), 3896–3905. <https://doi.org/10.1021/acssuschemeng.9b07368>.
- (9) Márquez-Montes, R. A.; Kawashima, K.; Vo, K. M.; Chávez-Flores, D.; Collins-Martínez, V. H.; Mullins, C. B.; Ramos-Sánchez, V. H. Simultaneous Sulfite Electrolysis and Hydrogen Production Using Ni Foam-Based Three-Dimensional Electrodes. *Environ. Sci. Technol.* **2020**, *54* (19), 12511–12520. <https://doi.org/10.1021/acs.est.0c04190>.